AFRL-DE-
TR-2000-1008

Band Structure Engineering of the Carrier-Induced Refractive Index in High-Power Midwave-Infrared Laser Diodes

Thomas F. Boggess
Michael E. Flatte'
Thomas C. Hasenberg
Winston K. Chan

The University of Iowa
Division of Sponsored Programs
2 Gilmore Hall
Iowa City, IA 52242

28 Mar 00

Final Report

APPROVED FOR PUBLIC RELEASE; DISTRIBUTION IS UNLIMITED.

AIR FORCE RESEARCH LABORATORY
Directed Energy Directorate
3550 Aberdeen Ave SE
AIR FORCE MATERIEL COMMAND
KIRTLAND AIR FORCE BASE, NM 87117-5776

AFRL-DE-TR-2000-1008

Using Government drawings, specifications, or other data included in this document for any purpose other than Government procurement does not in any way obligate the U.S. Government. The fact that the Government formulated or supplied the drawings, specifications, or other data, does not license the holder or any other person or corporation; or convey any rights or permission to manufacture, use, or sell any patented invention that may relate to them.

This report has been reviewed by the Public Affairs Office and is releasable to the National Technical Information Service (NTIS). At NTIS, it will be available to the general public, including foreign nationals.

If you change your address, wish to be removed from this mailing list, or your organization no longer employs the addressee, please notify AFRL/DELS, 3550 Aberdeen Ave SE, Kirtland AFB, NM 87117-5776.

Do not return copies of this report unless contractual obligations or notice on a specific document requires its return.

This report has been approved for publication.

SYLVIA DORATO, DR-III
Project Manager

FOR THE COMMANDER

HARRO ACKERMANN, DR-IV
Chief, Laser Division

R. EARL GOOD, SES
Director, Directed Energy

REPORT DOCUMENTATION PAGE

Form Approved
OMB No. 0704-0188

1. REPORT DATE *(DD-MM-YYYY)*	2. REPORT TYPE	3. DATES COVERED *(From - To)*
28/03/2000	Final Report	01-04-1997 to 29-02-2000

4. TITLE AND SUBTITLE

Band Structure Engineering of the Carrier-Induced Refractive Index in High-Power Midwave-Infrared Laser Diodes

5a. CONTRACT NUMBER
F29601-97-C-0041

5b. GRANT NUMBER

5c. PROGRAM ELEMENT NUMBER
62601F/63605F

6. AUTHOR(S)

Thomas F. Boggess, Michael E. Flatte',
Thomas C. Hasenberg and Winston K. Chan

5d. PROJECT NUMBER
3151

5e. TASK NUMBER
LC

5f. WORK UNIT NUMBER
DM

7. PERFORMING ORGANIZATION NAME(S) AND ADDRESS(ES)

The University of Iowa
Div. of Sponsored Programs
2 Gilmore Hall
Iowa City, IA 52242

8. PERFORMING ORGANIZATION REPORT NUMBER

9. SPONSORING / MONITORING AGENCY NAME(S) AND ADDRESS(ES)

AFRL/DELS
3550 Aberdeen Ave SE
Kirtland AFB NM 87117-5776

10. SPONSOR/MONITOR'S ACRONYM(S)

11. SPONSOR/MONITOR'S REPORT NUMBER(S)
AFRL-DE-TR-2000-1008

12. DISTRIBUTION / AVAILABILITY STATEMENT
DISTRIBUTION STATEMENT A, APPROVED FOR PUBLIC RELEASE; DISTRIBUTION UNLIMITED.

13. SUPPLEMENTARY NOTES

14. ABSTRACT

This program was aimed at developing the understanding of advanced type-II antimonide heterostructures required to realize high-power, room-temperature, diode lasers. The program incorporated elements of theory, semiconductor growth by molecular-beam epitaxy, ultrafast and continuous-wave optical characterization, and device processing, fabrication, and testing. Accomplishments include: 1) development of a highly-accurate 14-band k-dot-p band structure model and its application to calculations of Auger and radioactive recombination, gain and index spectra, and carrier transport, and to mid-infrared laser design, 2) measurements of Auger recombination, carrier transport, and gain and refractive index spectra in mid-infrared laser structures, 3) development of figures of merit for designing mid-infrared lasers, 4) design, growth, and characterization of optimized multiconstituent antimonide quantum wells for 3.5 micron lasers, and 5) the theoretical and experimental demonstration of superior Auger suppression in this structure.

15. SUBJECT TERMS
semiconductor laser, mid-infrared laser, laser diode, type-II superlattice, type-II quantum well, antimonides, band structure engineering

16. SECURITY CLASSIFICATION OF:			17. LIMITATION OF ABSTRACT	18. NUMBER OF PAGES	19a. NAME OF RESPONSIBLE PERSON
a. REPORT	b. ABSTRACT	c. THIS PAGE			Sylvia Dorato
Unclassified	Unclassified	Unclassified	Unlimited	68	19b. TELEPHONE NUMBER *(include area code)* (505) 846-4315

TABLE OF CONTENTS

LIST OF FIGURES

INTRODUCTION

This Final Report describes progress on developing an improved understanding of antimonide materials for midwave-infrared (MWIR) semiconductor lasers and the design, growth, and fabrication of such lasers. The report is organized into three sections. In the first, we describe our efforts related to the design, growth and fabrication of MWIR lasers. In the second, we focus on our efforts to develop and improve the understanding of the antimonide materials incorporated in these lasers. This section includes discussions of theory and measurements designed to address the nonlinear optical properties, carrier recombination, and carrier transport and capture in the type II quantum structures used for these lasers. Finally, we summarize and offer a self-evaluation and recommendations for future efforts in this area. The senior personnel and primary areas of responsibility are listed below:

University of Iowa (UI)

Professor Thomas F. Boggess, Principal Investigator: Development of MWIR ultrafast optical techniques and their application to measurements of optical and electronic properties of MWIR laser materials. Laser testing.

Professor Michael Flatté, Co-Principal Investigator: Theory of MWIR laser materials and laser design.

Professor Thomas C. Hasenberg, Co-Principal Investigator: Laser design and MBE growth.

Professor Winston Chan, Co-Principal Investigator: Processing and fabrication of MWIR lasers.

University of Illinois at Chicago (UIC)

Professor Christoph Grein: Calculations of Auger coefficients in MWIR laser materials.

The primary thrust of the program has been directed at developing the necessary understanding of type II antimonide materials in order to realize high-power, diode lasers operating at room temperature. The keys to high-power and high-temperature operation of diode

lasers are 1) suppression of Auger recombination for low-threshold operation, 2) suppression of intersubband absorption and other contributions to optical loss to achieve large slope efficiency, 3) low linewidth enhancement factors for suppression of filamentation, 4) efficient transfer of injected charge carriers into the laser active region, 5) control of series resistance to minimize Ohmic heating, 6) good thermal management to transfer heat from the laser, and 7) the integration of all of these factors within a single device without serious compromise in any single area. Satisfying these requirements is a formidable task and one that we have attempted to address on this program.

Theoretical efforts have focused on electronic structure engineering of superlattices and quantum wells with suppressed Auger recombination and intersubband absorption, the accurate calculation of band structures, Auger and radiative recombination, gain and density-dependent refractive index spectra, carrier transport, and figures of merit for laser performance. Experimental efforts have been based on two novel MWIR ultrafast optical systems, an optical parametric oscillator[1] (OPO) that produces subpicosecond pulses from ~ 1 to 4.5 μm and a photoluminescence upconversion system[2, 3] that has subpicosecond resolution from 1 to 5 μm. These systems have been used to measure all of the calculated properties mentioned above. These efforts have been supported by in-house MBE growth and device processing. In addition, both the theoretical and experimental techniques have been applied routinely to materials from other laboratories. In this Final Report, we summarize our efforts in each of these areas.

MBE GROWTH AND LASER PROCESSING

Since the beginning of this contract, we have brought on line two MBE machines – a Perkin Elmer model 430P and an EPI model 930. The Perkin Elmer 430P was a gift from Hughes Research Laboratories (HRL) to the University of Iowa and is the same machine that was used at HRL to grow MWIR lasers successfully. The latter MBE machine is new and was purchased with Prof. Hasenberg's start-up funds, which were provided by the University of Iowa. The EPI machine is equipped with state-of-the-art Sumo (made by EPI) effusion cells which greatly reduce growth rate transients. The presence of these so-called flux transients make it difficult to grow superlattices with repeatable layer thicknesses. Furthermore, the presence of flux transients requires a new set of calibration samples whenever the superlattice layer

thicknesses are changed. These layer thicknesses must be changed whenever a new laser wavelength is desired. The SUMO cells reduce the flux transients and hence eliminate the need for these extra calibration samples. The University of Iowa also provided the funds necessary to purchase an antimony valved cracker for the EPI 930 MBE machine. This machine was previously equipped with a conventional antimony cracking cell and an arsenic valved cracker. The addition of the antimony valved cracker allows us to grow InAs layers in MWIR superlattices with the antimony valve closed and the GaInSb layers with the arsenic valve closed. This results in structures with excellent crystalline quality, thereby suppressing the Shockley-Read recombination due to the Group V intermixing. In addition, the antimony capacity is twice that of the previous conventional cracking cell. Therefore, we can grow twice as much material before breaking vacuum and reloading antimony. In addition, closing the valve on the new cell allows us to conserve antimony as the cell is heating or as thick arsenide layers are being grown. This reduces undesirable antimony coating inside the machine.

Double heterostructures with InAs/AlAsSb/InAs/GaInSb BGQWs and InAs/AlGaSb SL barriers have been grown at UI using the EPI 930. Excellent structural quality has been obtained as exhibited by the X-ray diffraction data (funds for a high-resolution X-ray diffractometer were provided by the UI). Furthermore, we observe strong room temperature PL from these structures, indicating high quality material suitable for laser active regions. Examples of data obtained on structures grown in this machine are given in the next Section of this Report.

While excellent material has been grown in the EPI machine, we have not yet successfully grown a functional diode laser at UI (although structures grown in the Perkin-Elmer machine by Prof. Hasenberg while at HRL have been successfully, processed and tested at UI). This failure is largely a consequence of numerous machine breakdowns that have prevented meaningful iterations on laser design, growth, and testing. Our strategy from the outset was to utilize the EPI machine (rather than the Perkin Elmer) for laser growth due to the various state-of-the-art capabilities associated with it, as mentioned above. Unfortunately, this new machine has been subject to failures ranging from numerous leaks, to bad bearings in the substrate rotation stage, to shutter failures, and most recently to a leak in a water line. In many instances, long periods of successful calibration and test-sample growth and evaluation were followed by long periods of down time due to these breakdowns. In response to continuing problems with the EPI machine, we have returned the conventional antimony cracking cell to the Perkin Elmer

machine (this was originally taken from the Perkin Elmer to use on the new EPI machine, but became redundant with the purchase of the valved antimony cracker), and we can now grow antimonide materials in both machines.

During this contract, we have also established the capability to fabricate semiconductor lasers at the University of Iowa. The major fabrication facilities in our laboratories include photolithography equipment, thin film deposition by e-beam, thermal evaporation, and plasma-enhanced chemical vapor deposition, as well as etching capabilities, including reactive ion etching and ion beam etching. We also have the capability to attach and wirebond laser dies to a header for testing (funds from the UI were used to purchase a new wire bonder). Broad-area InAs/GaInSb-based diode lasers grown at HRL have been successfully processed and tested using these facilities.

LASER DESIGN, MODELING, GROWTH, FABRICATION, AND TESTING

Background

Laser design on this program was based on prior work done under Air Force support and in collaboration with Hughes Research Laboratories. This effort focused on InAs/$Ga_{.75}In_{.25}Sb$ (Type-II misaligned) broken-gap superlattices (BGSLs) as the laser active regions. Layer thicknesses and compositions were chosen based on 8-band **K•p** calculations. An attempt was made to minimize the density of states at the valence band edge, thereby reducing the laser threshold carrier density, and to eliminate final states for Auger and intersubband processes within the conduction and valence bands[4, 5]. Another contribution of this early effort was the development of InAs/AlSb SL cladding layers for MWIR lasers. These cladding layers are more reproducible than alloy clads and can be grown both n^+ and p^+ using standard Si and Be dopants and are now commonly employed in MWIR interband laser designs.

In 1995, our program contributed to the demonstration by Hughes Research Laboratories (HRL) of the first MWIR laser diodes based on InAs/GaInSb SLs.[6] It was necessary to grow MQWs consisting of short segments (10 periods or less) of these SLs bounded by InGaAsSb barriers because the 2-layer BGSL wells have a high degree of compressive strain. The InGaAsSb barriers were grown with tensile strain to yield a strain balanced well/barrier combination. Numerous laser diodes were demonstrated over a wide range of MWIR

wavelengths including 2.8 μm, 3.1 μm, 3.2 μm, 3.4 μm, 4.1 μm, and 4.3 μm diodes.[7] Pulsed laser operation was observed up to 255K with 3.2 μm devices of this design with a threshold current density of 760 A/cm^2 at 140 K. CW operation was achieved for temperatures up to 180K, but it should be noted that no attempt was made at thermal management. A similar BGSL MQW sample lased up to 110 K at 4.32 μm with a threshold current density of 4.9 kA/cm^2.

In the mean time, both theoretical and experimental tools were applied to engineer and investigate the optical and electronic properties of these structures. These studies revealed that the termination of the SL segments with the quaternary barriers seriously degraded the optimizations that had been designed into the SL itself. Specifically, Auger rates comparable to that expected for Type-I structures were measured and barrier states were predicted to yield excessive intersubband absorption at wavelengths near the band edge. This led us to consider alternative designs.

The Four-Layer Broken-Gap Superlattice Laser

In the second generation of SL active region lasers, the barrier layer was thinned and chosen as a strain-balancing quinternary, thereby yielding an InAs/$Ga_{.60}In_{.40}Sb$/InAs/InGaAlAsSb 4-layer BGSL. The utilization of the quinternary allows the use of a more heavily strained GaInSb layer and strain balancing over a single period of the SL. Relative to AlSb barrier layers used in W laser designs, the quinternary layers also added more flexibility for the optimal tailoring of valence band states for suppression of Auger recombination and intersubband absorption. The band edge diagram and band structure of a 4-μm-band-gap 4-layer BGSL are shown in Fig. 1. Other wavelengths are readily achievable with this basic structure by simply varying layer thicknesses. As the 4-layer BGSL's were developed, our band structure code was upgraded to include a 14-band bulk basis set. This resulted in substantially more accurate valence subband structure.

Double heterostructure laser diodes for 2.7, 3.7 and 5.2 μm wavelength operation were fabricated using thick 4-layer BGSL active regions. The 2.7 μm device lased under electrical injection, but the longer wavelength devices lased only when optically pumped. We believe this is a consequence of poor hole transport in these structures. The longer wavelength devices required thicker quinternary layers for strain balancing. These layers provided extremely strong hole confinement in the GaInSb layers and, hence, poor cross-well transport. Although these

structures were diodes that were not optimized for optical pumping, the 3.7 μm and 5.2 μm devices lased up to 300 K and 185 K, respectively, when optically pumped.[8]

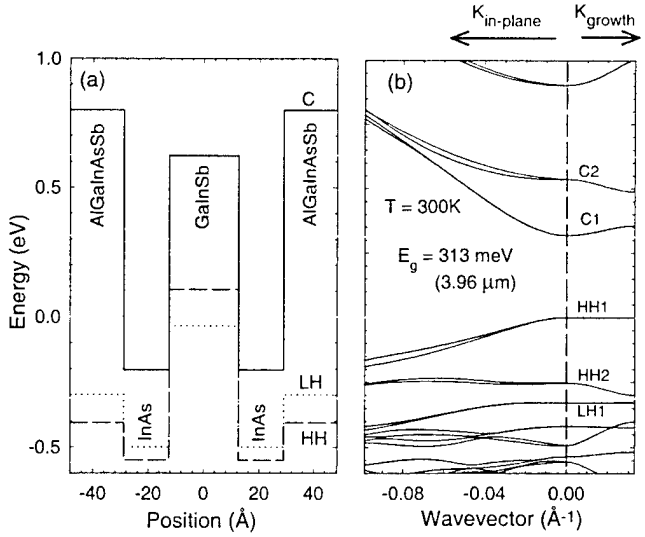

*Figure 1. Band alignment (left) and band structure (computed with a 14-band superlattice **K•p** model) of 4-layer superlattice.*

Portions of the 2.7-μm device structures (TCH1633) were processed and fabricated into lasers at UI. One of these devices lased under electrical injection for duty cycles of over 25% (no effort was made to optimize heat dissipation). Results for TCH 1633 at 80K are shown in Fig. 2. The laser was fabricated using silver epoxy for die attach. This approach was replaced with indium bonding in later laser fabrication. The duty cycle for the data in Fig. 2 is either 1% or 0.1% and the pulse width was 1 μs. The difference between 1% and 0.1% runs is probably due to steady-state resistive heating of the cold-finger. No evidence of facet damage was observed in these diodes at low temperatures. The peak power per facet is approximately 160 mW for this laser.

We also investigated the temperature dependence of this laser (again with silver epoxy die attach) over the range of 80 to 190 K. These results, which are shown below in Fig. 3, were obtained using 5 μs pulses and a 0.1% duty cycle. Lasing was clearly observed up to 190 K. From these data, we can extract T_0, as shown in Fig. 4. We observe two distinct regions: 1) at and below 150 K we extract $T_0 = 54$ K. Above 150 K, T_0 decreases to 29 K. A device that was indium bonded later lased at temperatures up to 220 K.

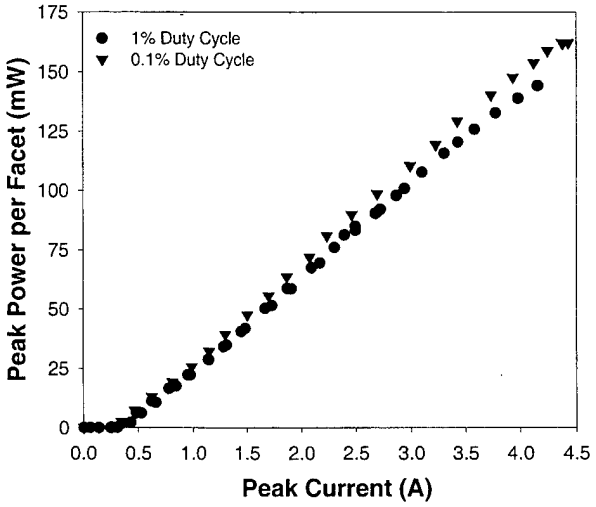

Figure 2. L-I curve for TCH1633 at 80 K for 1% and 0.1% duty cycles.

Measurements were also performed as a function of duty cycle. We found, as seen in Fig. 5, that the output power was affected only modestly upon increasing the duty cycle from 1% to 8%. Above 8%, however, the output power began to decrease dramatically. Lasing was observed up to a maximum of 25% duty cycle. For comparison, using silver paint for the die attach, no lasing was observed for a duty cycle of 4%.

As discussed in detail in the next section, owing to the promising results obtained on the four-layer BGSL structures, considerable effort on the current program was directed toward understanding their optical and electrical properties. Such studies are relevant not only to the four-layer BGSLs, but also to the closely related W-laser active regions pioneered by Naval Research Laboratories. Still, for diode lasers, it was clear that the large band offsets in the four-layer BGSL structures (and the W-lasers) posed serious problems for carrier transport and injections.

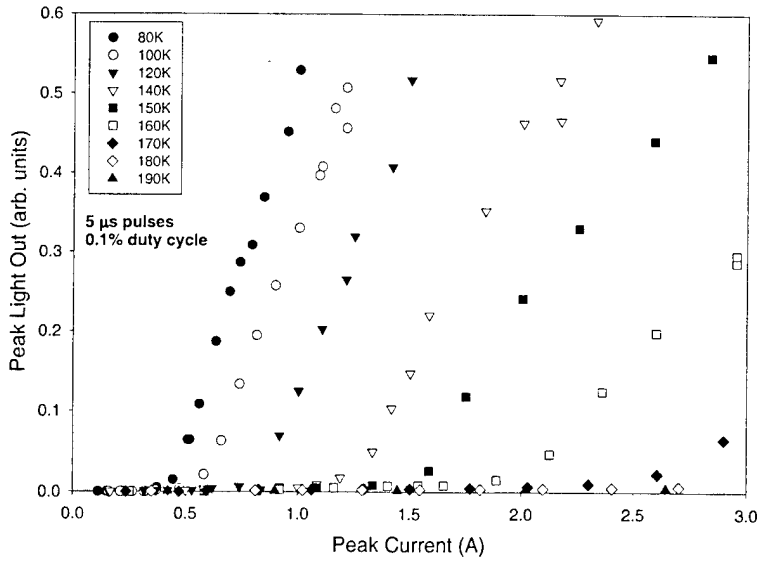

Figure 3. L-I curves for TCH1633 at various temperatures.

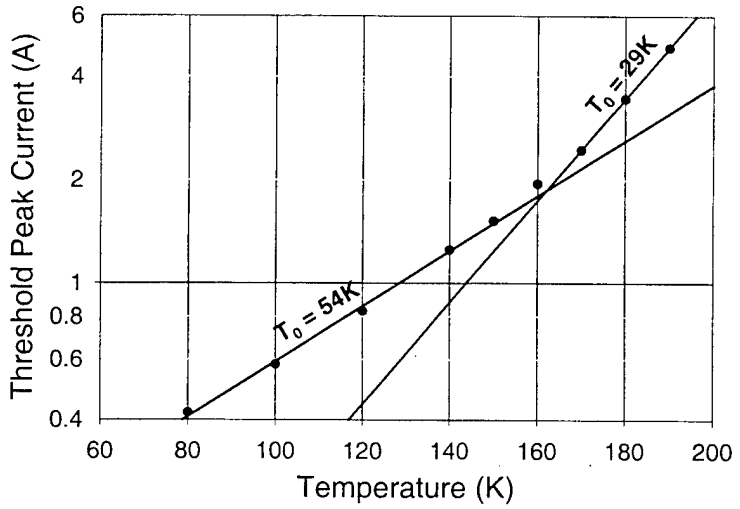

Figure 4. Threshold current as a function of temperature in TCH1633 to yield T_0.

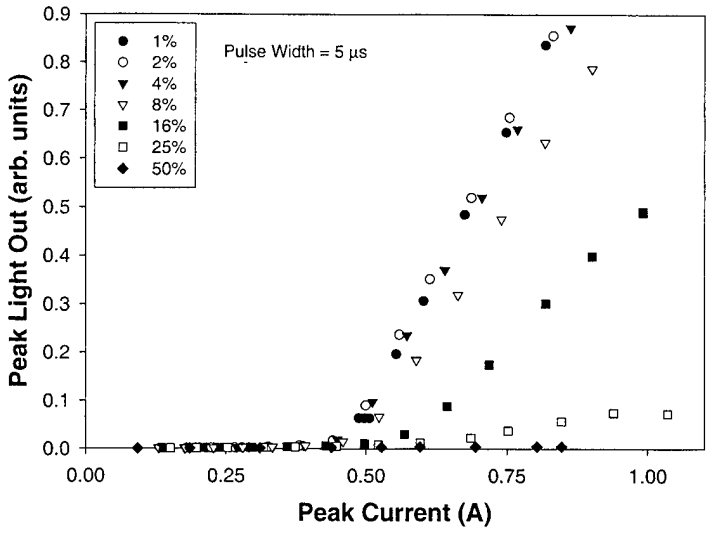

Figure 5. L-I curves for TCH 1633 for various duty cycles.

The Broken-Gap Quantum Well Laser

In response to this problem, we developed an integrated laser diode design for emission at 3.4 µm that successfully addresses both Auger recombination and vertical hole transport. The active region is found to theoretically have an Auger lifetime that is longer than typical Shockley-Read-Hall (SRH) lifetimes, even at room temperature. In addition, the active region, separate confinement region, and cladding regions are specifically designed for efficient electrical injection and vertical transport. Calculations indicate that the room temperature internal threshold current density for a single-quantum-well laser diode could be as low as 100 A/cm^2. Even if multiple wells are necessary due to large optical losses in the device, the threshold current density should be an order of magnitude smaller than previous type-II designs. We first describe the optoelectronic properties of the active region and subsequently the transport, injection, and confining properties of the separate confinement region (SCR) and clads.

The active region, which is referred to as a broken-gap quantum well (BGQW), is shown in Fig. 6. The electronic and optical properties of the material have been calculated using a 14-band superlattice **K·p** formalism. Earlier 8-band versions of this formalism have successfully predicted the density-dependent optical properties[9,10] and Auger rates [11]of superlattices based on the InAs/GaInSb material system. The active region has a well consisting of 21 Å $AlAs_{0.15}Sb_{0.85}$ / 15 Å InAs / 25 Å $Ga_{0.65}In_{0.35}Sb$ / 15 Å InAs / 21 Å $AlAs_{0.15}Sb_{0.85}$. The barrier surrounding the well is a 27 Å $Al_{0.60}Ga_{0.40}Sb$ / 11 Å InAs superlattice.

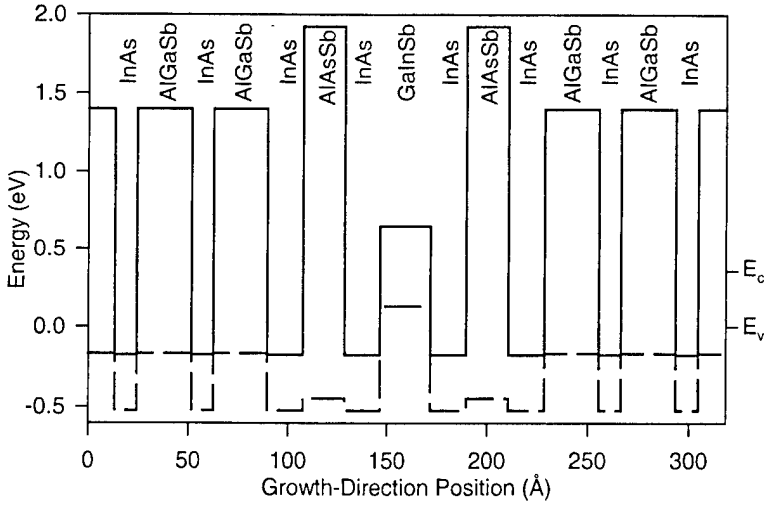

Figure 6. Bulk band edge energies as a function of growth direction position. The solid line is the bulk conduction band edge and the dashed line is the bulk heavy-hole edge. The conduction and valence energies of the superlattice are shown on the right of the figure.

This active region structure demonstrates both band-edge and final-state optimization, but the most significant improvement relative to previous designs is in the final-state optimization of Auger recombination.[12] Band-edge optimizations (balancing the conduction and valence band-edge densities of states) require moderate band offsets among material constituents and lead to a large differential gain and a small linewidth enhancement factor.[4, 10, 13] Final-state suppression of intersubband absorption requires control of vertical transitions with energy equal to the lasing energy. This requires even larger band offsets in order to affect states approximately one energy gap from the band edges, and has been achieved in broken-gap designs already.[5, 13] Suppression of intersubband absorption improves the slope efficiency of the device, and optimized designs have active region material slope efficiencies (ratio of net material gain to total material gain) close to 100%.[14]

The most difficult processes to suppress are the Auger processes, because they involve substantial momentum transfer between carriers. Calculations of the hole-hole Auger process show that the most probable transitions involve final states with large in-plane wavevectors ($K_{in\text{-}plane} \sim 0.05$ Å^{-1}). Because of this, optimization strategies that rely on creating gaps in the electronic structure at zone center are not fully effective. By creating a gap in the electronic structure at wavevectors that are involved in the most probable Auger transitions, the calculated

Auger rate in the BGQW is suppressed by a factor of 30 with respect to comparable 4-layer BGSL's.

This is illustrated in Fig. 7, where the initial and final states of the holes involved in the most probable hole Auger processes are shown for the BGQW and for the 4-μm, 4-layer, BGSL. The band structure is shown in the in-plane direction for all possible growth-direction momenta, yielding shaded bands of states. The intensity of a plotted point is proportional to its overlap with the top heavy-hole state at $K_{in\text{-}plane} = 0.02$ Å^{-1}; thus, strongly coupled states appear dark. There is a significantly larger gap in the electronic structure at energies around –450 meV and in-plane wavevectors of ~0.05 Å^{-1} for the BGQW structure than for the 4-layer BGSL. This leads to suppression of the Auger process, as is evidenced by the absence of transitions in the BGQW to states with energy around -450 meV. The resulting Auger rate at room temperature at the optimal density for lasing is 0.06 ns^{-1}. Because this rate is much smaller than the typical 0.3 ns^{-1} rate from SRH processes, the system is expected to be SRH-limited at room temperature. The total carrier lifetime at the optimum density for lasing is 2.5 ns, which is six times longer than for the 4-layer BGSL.

The dependence of the optimum lasing threshold of a device on the active region can be summarized with a cavity-independent figure of merit: the optimal ratio of the net active region gain to the volumetric recombination current density.[14] Assuming a 3.0 ns SRH lifetime, the figure of merit for the BGQW is 2900 μm^2/A at 300K. This value far exceeds that of other mid-infrared materials (~40-75 for type-I quantum wells and ~260 for type-II superlattices). Because the threshold current density is inversely proportional to this figure of merit, lasing thresholds for this structure should be more than an order of magnitude smaller than current interband diodes. The large net material gain (625 cm^{-1}) at the optimal density suggests that a single quantum well active region should be sufficient for lasing in a suitably designed cavity. We now describe such a cavity.

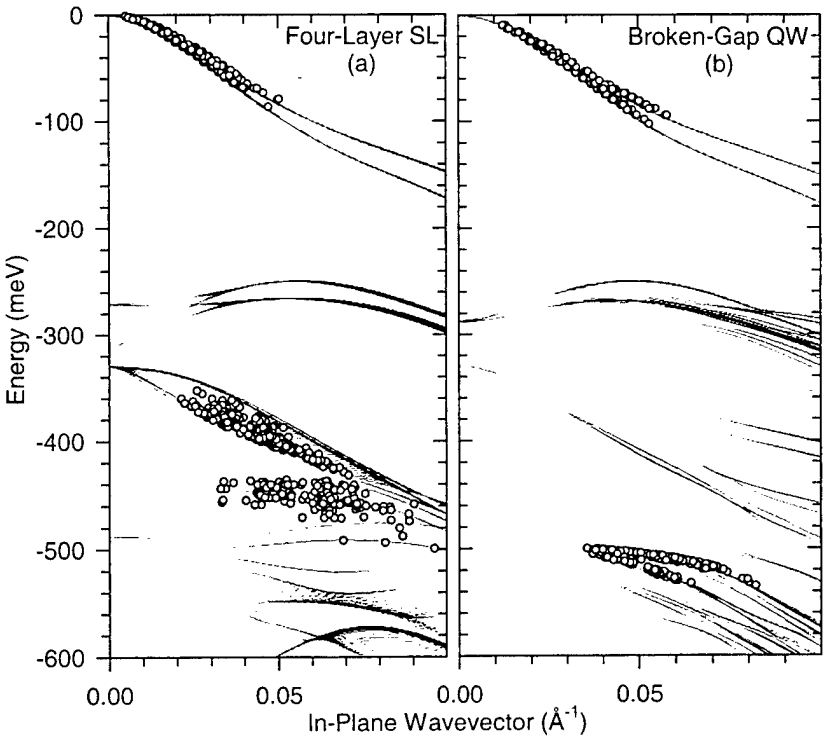

Figure 7. Initial and final energy and in-plane wavevector for the most probable hole-hole Auger transitions (open symbols) overlaid on the electronic structure of the valence band for (a) a four-layer superlattice and (b) the broken-gap quantum well. The density of the gray scale is proportional to the strength of the coupling of each point to states near the top of the valence band. The broken-gap quantum well has a larger gap in its electronic structure at $K_{in\text{-}plane} \sim 0.05$ Å^{-1} and $E \sim -50$ meV, which is the origin of its additional Auger suppression.

An essential feature of this cavity, which is shown in Fig. 8, is a SCR that reduces the mode overlap with the highly doped clads and has good hole mobility. The SCR of the cavity is 0.4 μm thick on the *n* side and 0.6 μm thick on the *p* side. Recent work in near-infrared diode development (2.0 – 2.7 μm) has demonstrated the importance of such SCR's for high-temperature and high-power operation.[15] The material used for the SCR is the same InAs/AlGaSb superlattice that is used as the quantum-well barrier in the active region. It is lattice matched to the GaSb substrate and has a larger index of refraction ($n \sim 3.45$) than that of the doped clads. The Boltzmann vertical mobility of holes in this superlattice is 160 cm^2/Vs for a 100 fs relaxation time and a doping level of 1×10^{17} cm^{-3}. This vertical hole mobility, which is comparable with that of bulk InAs and two orders of magnitude larger than that of the 4-layer BGSL, ensures good vertical transport between the clads and the active region. Because the SCR is a superlattice, it is straightforward to grade its band edges by varying the superlattice period.

This can be used to match the band-edges of the SCR to the injection level of the clads or to localize injected carriers near the active region.

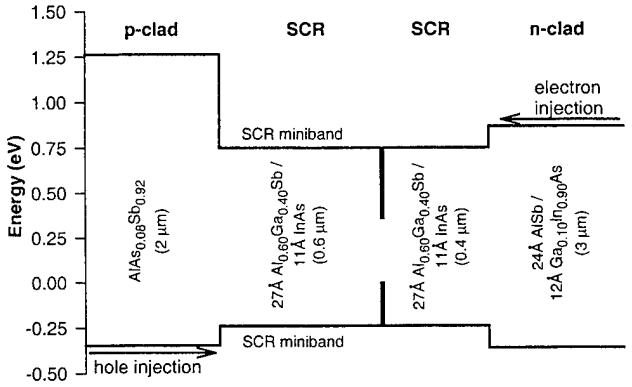

Figure 8. Schematic of the laser diode structure that includes a single quantum well active region, lightly-doped separate confinement regions (SCR), and heavily-doped clads. The estimated mode width and non-active-region modal losses for this structure are 1.3 µm and 20 cm^{-1}, respectively.

The $AlAs_{0.08}Sb_{0.92}$ *p* clad has a small index of refraction ($n \sim 3.23$), a large confining potential for electrons, and a well-matched hole injection level with the superlattice clad. The 24 Å AlSb / 12 Å $Ga_{0.10}In_{0.90}As$ superlattice *n* clad ($n \sim 3.33$) provides electron injection matched to the miniband of the separate confinement superlattice and allows *n*-doping with silicon.

Based on optical mode calculations for a 2-mm-long cavity with uncoated facets, we estimate the sum of the mirror losses (α_m) and *non-active-region* modal waveguide losses ($\langle \alpha_w \rangle$) for the cavity described above to be $\left(\alpha_m + \langle \alpha_w \rangle\right)$ = 20 cm^{-1}. The optical confinement factor is 2.3% for a single quantum well in this cavity. Because active region losses due to intersubband absorption are included in the calculation of the *net* active region gain, they are not included in the non-active-region cavity loss value. The calculated internal threshold current density for a *single quantum well* device is 100 A/cm^2. Recently, total modal losses of 50 cm^{-1} and 100 cm^{-1} have been observed in structures without separate confinement regions (these *total* loss values include intersubband absorption losses in the active region). [16, 17]

Table I presents internal threshold current densities for the BGQW active region at 300K for a series of cavity losses and numbers of wells. Even for the largest loss case (100 cm^{-1}), lasing is achievable with 4 wells at 810 A/cm^2. The use of few quantum wells significantly

reduces the problem of non-uniform carrier distribution in the active region. Finally, it is instructive to consider the threshold current density due to intrinsic processes (Auger and radiative recombination). This defines the ideal lower limit on the current density when the SRH lifetime becomes arbitrarily large. In this limit, the figure of merit is 5960 $\mu m^2/A$, and the ideal current density for a single quantum well device with a non-active-region loss of 20 cm^{-1} is 44 A/cm^2.

	$\alpha_m + \langle \alpha_w \rangle$		
Wells	**20 cm^{-1}**	**50 cm^{-1}**	**100 cm^{-1}**
1	102	–	–
2	97	404	–
3	119	228	–
4	145	227	808
5	171	242	510
7	224	286	447
10	303	362	485

Table I: Calculated internal threshold current density (A/cm^2) as a function of non-active-region optical loss and number of quantum wells. For each cavity, the minimum current density is boxed.

This laser design with the BGQW active region is calculated to have a factor of six increase in the carrier lifetimes at room temperature lasing densities with respect to a comparable 4-layer BGSL and is designed specifically for electrical injection. The theoretical threshold figure of merit for the active region is 2900 $\mu m^2/A$ at room temperature, while the slope efficiency figure of merit is 99.4% (see below for a more complete discussion of the figures of merit). The integrated separate confinement region superlattice has a hole vertical mobility of the same order as bulk InAs and well-matched band edges for transport. For a low-loss cavity, the internal threshold current density is expected to be as low as 100 A/cm^2 at room temperature for a single quantum well diode emitting at 3.4 μm.

We have grown BGQWs with excellent structural quality as evidenced by strong room-temperature PL and sharp features in high resolution X-ray diffraction (see Fig. 9). However, we have yet to demonstrate the successful operation of a diode laser based on the BGQW active region. This is in large part due to a series of breakdowns in our new EPI-930 MBE machine. However, several BGQW lasers have been grown, processed, and tested with negative results. All have been characterized by unacceptably large series resistance, which may indicate a

vertical transport problem due to a mismatch between the superlattice barrier states and the quantum well states. The question of whether this mismatch is a consequence of growth errors or errors in the theoretical design arising, e.g., from uncertainties in input parameters remains open. The answer to this question will require additional iterations of growth and characterization. We also note that measurements on the BGQW (discussed below) suggest that the recombination rates and gain in the as-grown structures are not yet meeting theoretical expectations. On the other hand, the measured Auger rates in the BGQW are still significantly lower than those measured in the 4-layer BGSL.

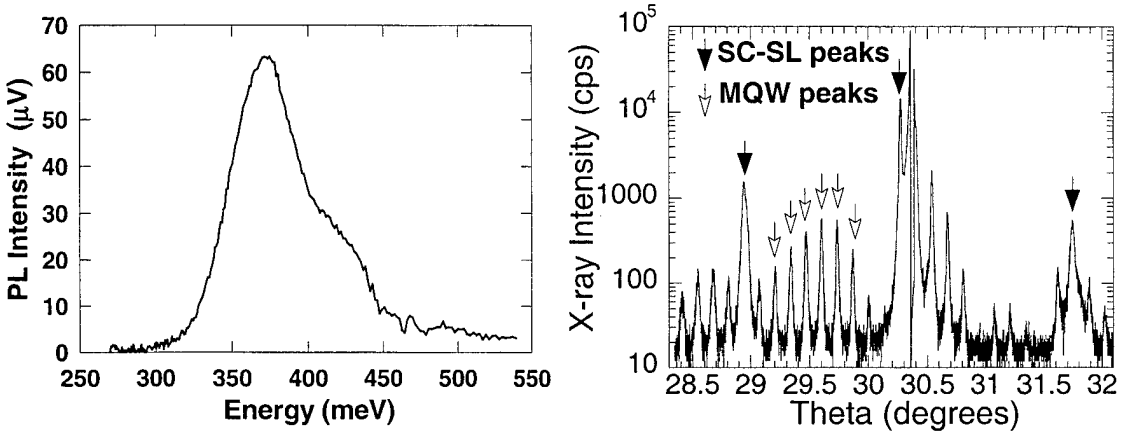

Figure 9. Room-temperature PL and high-resolution X-ray diffraction for a 3.5 μm BGQW.

Figures of Merit

The threshold and slope-efficiency figures of merit are quantities that we have evolved from the work of Coldren and Corzine.[18] The threshold figure of merit, ξ_T, is the maximum net gain coefficient to volumetric current ratio. This is a quantity that is inversely proportional to the two-dimensional threshold current density and that depends only on the material properties of the active region. That is, it is completely independent of device properties. Hence, it is an extremely useful quantity for comparison of predicted thresholds for various active regions incorporated into identical cavities. The threshold figure of merit can be used to determine an optimal active region thickness for a given set of cavity parameters. A second figure of merit that is more relevant to output power is the slope efficiency figure of merit, ξ_S, which is defined as the maximum of the ratio of the coefficients of net gain to gain. This figure of merit is again

independent of device details and is directly proportional to the ratio of the output power to the two-dimensional current density.

A comparison of the two figures of merit at room temperature and at the optimal carrier density for the three generations of active region designs (BGSL MQW, 4-layer BGSL, and BGQW) is given in Table II. These results are semi-emperical in that experimental Auger rates and gains were used. The optimal number of periods is also shown, as is the estimated room-temperature threshold current density. Shown for comparison are results for bulk InAs. The optimal active region thickness (or number of periods) is calculated assuming a 1.3 μm mode width and 20 cm^{-1} of internal loss. Although the optimal number of periods for the BGQW structure is 4, we find that operation with two wells is possible with only a modest penalty in threshold current density (specifically an increase from 0.76 to 1.25 kA/cm^2). In contrast, operation of the 4-layer BGSL with 2 periods requires 6 kA/cm^2. Further decreases in threshold current density could be achieved using a lower loss cavity or by operation at temperatures below 300K. This comparison illustrates clearly the progress that has been made toward optimizing MWIR laser active regions and the advantages of the BGQW active region design. It also demonstrates that, in a low-loss cavity, cross-well transport should not be an issue with this structure, as only two wells are required. This indicates that such structures should be superior to our previous 4-layer BGSL (as well as the W-laser) active regions for MWIR diode lasers. We emphasize that the figures of merit in Table II were arrived at using experimental values for recombination and gain. Theory predicts a threshold figure of merit for the BGQW that is nearly an order of magnitude larger, with a corresponding decrease in threshold current density.

	ξ_T ($\mu m^2/A$)	ξ_S (%)	# periods	J_{th} (kA/cm^2)
InAs	5.7	88	2500Å	46
BGSL MQW	11.8	37	4	22
4-layer BGSL	137	97	5	1.9
BGQW	350	99	4	0.76

Table II. Figures of merit, optimal number of periods, and predicted 300K threshold current density for four structures with 300K band gaps near 4 μm.

Optically-Pumped Structures Based on the BGQW

Given the large threshold and slope efficiency figures of merit associated with the BGQW active regions and the fact that failure of the initial diode lasers based on this structure is likely related to vertical transport issues, we have considered the incorporation of the BGQW into laser structures designed for optical pumping. What follows is a summary of several preliminary structures designed for optical pumping at either 1.55 μm or at 2 μm. The following assumptions have been made in this analysis. 1) The waveguide losses in the clad and separate absorbing regions (SAR) are 10 cm^{-1}. The materials are all undoped, so these losses should be small. All calculations assume a SRH lifetime of 3 ns. The Auger coefficient is the experimental coefficient from the 4-μm, 4-layer BGSL ($2.4x10^{-27}$ cm^6/s) scaled by the square of the superlattice period. This should be a conservative estimate. The theoretical gain is used in the calculations. Values for threshold intensity are the *incident* values required to reach threshold. The intensity in the structure is assumed to be 60% of this value as a consequence of Fresnel losses. We note that AR coatings and an optically-pumped injection-cavity (OPIC)[19] design would yield additional improvements. The tables below provide the waveguide width (WG), the total loss $<\alpha_{total}>$, the ratio of the mirror loss $<\alpha_m>$ to the total loss, the percent absorption of the pump light in the SAR, the optimal number of quantum wells, the equivalent threshold current density (J_{2D}), and the threshold pumping intensity (I_{th}).

1.55 μm Pumping

Structure 1

Wavelength: 4.4 μm

SAR: 12Å InAs/9 Al50Ga40In10Sb (α at 1.55 μm = 6000 cm^{-1})

BGQW: 17Å InAs/12 AlSb/22 InAs/25 Ga70In30Sb/22 InAs/12 AlSb/17 InAs

Auger coefficient: $22x10^{-27}$ cm^6/s

Figures of Merit: 385 $\mu m^2/A$, 95% at $2.5x10^{17}$ cm^{-3}

WG (μm)	$\langle \alpha_{total} \rangle$ (cm^{-1})	$\frac{\langle \alpha_m \rangle}{\langle \alpha_{total} \rangle}$ (%)	SAR Abs (%)	Num QW's	J_{2D} (kA/cm^2)	I_{th} kW/cm^2
2.0	20.6	58.1	70	4	1.09	1.5
1.5	20.4	58.8	59	3	1.08	1.5
1.0	20.2	59.5	45	3	12.1	1.6
0.5	20.2	59.3	26	3	21.9	3.0

Structure 2

Wavelength: 4.2 μm

SAR: 18Å InAs/9 Al45Ga40In15Sb (α at 1.55 μm = 10,000 cm^{-1})

BGQW: 18Å InAs/12 AlSb/22 InAs/22 Ga70In30Sb/22 InAs/12 AlSb/18 InAs

Auger coefficient: 29x10^{-27} cm^6/s

Figures of Merit: 185 μm^2/A, 92% at 3.0x10^{17} cm^{-3}

WG (μm)	$\langle \alpha_{total} \rangle$ (cm^{-1})	$\frac{\langle \alpha_m \rangle}{\langle \alpha_{total} \rangle}$ (%)	SAR Abs (%)	Num QW's	J_{2D} (kA/cm^2)	I_{th} kW/cm^2
2.0	20.6	58.1	86	5	2.3	3.2
1.5	20.4	58.8	78	4	2.2	3.0
1.0	20.2	59.5	63	3	2.3	3.1
0.5	20.2	59.3	39	3	3.8	5.2

Structure 3

Wavelength: 4.1 μm

SAR: 18Å InAs/ 11 Al60Ga30In10Sb (α at 1.55 μm = 7800 cm^{-1})

BGQW: 19Å InAs/12 AlSb/21 InAs/20 Ga60In40Sb/21 InAs/12 AlSb/19 InAs

Auger coefficient: 31×10^{-27} cm^6/s

Figures of Merit: 390 μm^2/A, 93% at 2.25×10^{17} cm^{-3}

WG (μm)	$\langle \alpha_{total} \rangle$ (cm^{-1})	$\frac{\langle \alpha_m \rangle}{\langle \alpha_{total} \rangle}$ (%)	SAR Abs (%)	Num QW's	J_{2D} (kA/cm^2)	I_{th} kW/cm^2
2.0	20.6	58.1	79	4	0.79	1.4
1.5	20.4	58.8	69	3	0.66	1.3
1.0	20.2	59.5	54	3	0.57	1.4
0.5	20.2	59.3	32	3	0.59	2.5

2 μm Pumping

Structure 1 (same as Structure 2 for 1.55μm pumping)

Wavelength: 4.2 μm

SAR: 18Å InAs/9 Al45Ga40In15Sb (α at 1.55 μm = 10,000 cm^{-1})

BGQW: 18Å InAs/12 AlSb/22 InAs/22 Ga70In30Sb/22 InAs/12 AlSb/18 InAs

Auger coefficient: 29×10^{-27} cm^6/s

Figures of Merit: 185 μm^2/A, 92% at 3.0×10^{17} cm^{-3}

WG (μm)	$\langle \alpha_{total} \rangle$ (cm^{-1})	$\frac{\langle \alpha_m \rangle}{\langle \alpha_{total} \rangle}$ (%)	SAR Abs (%)	Num QW's	J_{2D} (kA/cm^2)	I_{th} kW/cm^2
2.0	20.6	58.1	27	5	2.0	7.7
1.5	20.4	58.8	21	4	1.7	8.3
1.0	20.2	59.5	14	3	1.4	10.3
0.5	20.2	59.3	7	3	1.5	20.5

Structure 2

Wavelength: 4.1 μm

SAR: 18Å InAs/ 9 Al40Ga43In17Sb (α at 2.06 μm = 3000 cm^{-1})

BGQW: 19Å InAs/12 AlSb/23 InAs/20 Ga75In25Sb/23 InAs/12 AlSb/19 InAs

Auger coefficient: $29x10^{-27}$ cm^6/s

Figures of Merit: 160 $\mu m^2/A$, 93% at $3.0x10^{17}$ cm^{-3}

WG (μm)	$\langle \alpha_{total} \rangle$ (cm^{-1})	$\frac{\langle \alpha_m \rangle}{\langle \alpha_{total} \rangle}$ (%)	SAR Abs (%)	Num QW's	J_{2D} (kA/cm^2)	I_{th} kW/cm^2
2.0	20.6	58.1	45	4	1.9	4.3
1.5	20.4	58.8	36	4	1.6	4.5
1.0	20.2	59.5	26	3	1.4	5.4
0.5	20.2	59.3	14	3	1.4	10.4

ADVANCES IN THE UNDERSTANDING OF BROKEN-GAP MATERIALS

Background

By closely coupling state-of-the-art theoretical modeling and measurements, we have made significant contributions to the knowledge base for antimonide broken-gap quantum structures. As part of this program, a 14-band superlattice **K·p** formalism has been developed and compared in detail to optical measurements of various physical material properties. Experiments have been based primarily on either time-resolved differential transmission (pump-probe) using our ultrafast OPO or on time-resolved photoluminescence (PL) upconversion. Schematic diagrams of illustrating the two techniques are shown in Fig. 10. This work may be loosely classified into work related to changes in the optical properties of these structures with carrier injection, carrier recombination, carrier transport and capture.

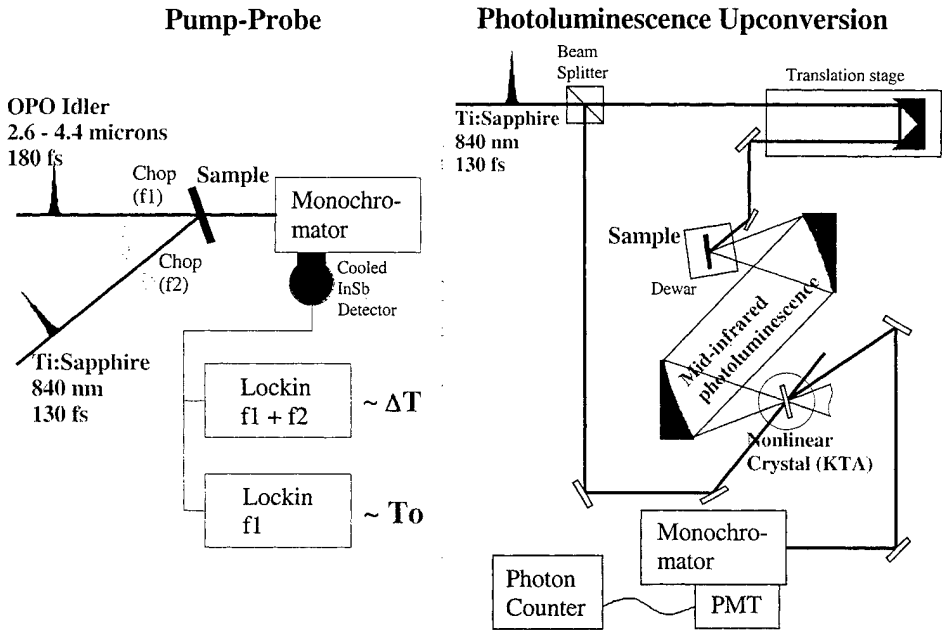

Figure 10. Schematic diagrams of pump-probe and photoluminescence upconversion experimental arrangements.

Carrier Induced Changes in Optical Properties

Linewidth Enhancement Factor - Theory

Many of the potential applications for mid-infrared semiconductor lasers, in particular those involving molecular spectroscopy and remote sensing, require coherent sources with narrow linewidths. Spectral purity in a semiconductor laser is degraded by the coupling between phase and amplitude noise such that the linewidth is broadened beyond the Schawlow-Townes limit according to[20]

$$\Delta\nu = \Delta\nu_0\left(1+\alpha_{lwe}^2\right), \qquad (1)$$

where $\Delta\nu_0$ is the Schawlow-Townes linewidth and α_{lwe} is the linewidth enhancement factor. The linewidth enhancement factor is also a measure of the likelihood of formation of optical filaments. At high powers, optical filamentation can lead to catastrophic facet damage in the

localized optical fields. Devices with small linewidth enhancement factors have the capability of producing larger output powers without facet damage.

The linewidth enhancement factor (α_{lwe}) is defined as the ratio of the density derivative of the real (χ_r) and imaginary (χ_i) parts of the complex susceptibility. However, when the fractional change in the index of refraction is small compared to the fractional change of the absorption coefficient, the linewidth enhancement factor can be written in terms of the density derivatives of the index of refraction (n) and the net gain (γ_{net}),

$$\alpha_{lwe}(\omega) = \frac{d\chi_r(\omega)/dN}{d\chi_i(\omega)/dN} \approx -\frac{4\pi}{\lambda}\frac{dn(\omega)/dN}{d\gamma_{net}(\omega)/dN}, \qquad (2)$$

where N is the carrier density and ω is the lasing frequency. The net gain, γ_{net}, differs from the fundamental gain due to the presence of intersubband absorption, which can be significant in mid-infrared materials. Because dn/dN can be related to the differential gain spectrum by a Kramers-Krönig transformation, the linewidth enhancement factor can be written entirely in terms of the differential gain spectrum,

$$\alpha_{lwe}(\omega) = 4\omega\frac{\int_0^\infty \left(\frac{d\gamma_{net}(\omega')/dN}{\omega'^2-\omega^2}\right)d\omega'}{d\gamma_{net}(\omega)/dN}, \qquad (3)$$

or, equivalently,

$$\alpha_{lwe}(\omega) = 4\omega\int_0^\infty \frac{\left[\frac{d\gamma_{net}(\omega')/dN}{d\gamma_{net}(\omega)/dN}\right]}{\omega'^2-\omega^2}d\omega'. \qquad (4)$$

The quantity in square braces in Eq. 4 is the differential gain spectrum *relative* to the magnitude of the differential gain at the lasing wavelength. When written in this form, the linewidth enhancement factor is a function only of the shape of the relative differential gain spectrum. Thus, we can compare material systems of comparable band gaps using their relative differential gain spectra.

Whereas dn / dN (and hence, α_{lwe}) vanishes near the peak of the *differential* gain spectrum due to the symmetry of the Kramers-Krönig transform, lasers typically operate at the frequency of the peak of the gain spectrum. In interband semiconductor lasers, as contrasted with atomic-like lasers, the peak of the differential gain is shifted away from the peak of the gain due to the opposite curvature of the conduction and valence bands. This shift is increased by any imbalance between conduction and valence band densities of states.[21,22] Because of this, semiconductor lasers typically have linewidth enhancement factors significantly different from zero. Typical values for near-infrared semiconductor lasers range from 2 – 6.[23,24]

Three primary strategies have been employed for reducing the linewidth enhancement factor in near-infrared lasers. The first is to reduce the imbalance between the conduction and valence band densities of states through the use of strain and quantum confinement.[21,25] Reducing the density of states imbalance increases the differential gain at the lasing energy and decreases the width of the differential gain spectrum. The second strategy is to p-dope the active region, which helps to offset the density of states imbalance.[21,22,25] Third, a distributed feedback grating (DFB) can be used to detune the lasing energy from the peak of the gain towards the peak of the differential gain.[22,26] The amount of detuning that can be used is limited by the range of energies over which there is positive gain. When the peak of the differential gain spectrum lies in the region of positive gain, it is possible to reduce the linewidth enhancement factor to near zero.

The situation is more challenging in the mid-infrared since the conduction band effective mass (of a bulk material) decreases roughly proportionally with the band gap, increasing the density of states imbalance. In addition, p-doping the active region aggravates existing problems with Auger recombination. Thus, producing semiconductor lasers with small linewidth enhancement factors requires careful attention to the problem of density of states mismatch. There have been relatively few reports of linewidth enhancement values for wavelengths beyond 1.55 μm. Meyer, *et al.*, report calculated values of 1.7 and 4.2 for early mid-infrared type-II quantum wells and superlattices.[13] Vurgaftman has reported a calculated value of 1.1 for the type-II quantum well[27] of Ref. [13]. Recently, Anson, *et al.*, reported measurements of small linewidth enhancement factors (< 1.0) in a 4 μm type-II superlattice.[10] Intersubband quantum cascade lasers are expected to have ultra-low linewidth enhancement factors (<0.1) due to the extremely narrow joint density of states characteristic of atomic-like systems.[28]

We have performed calculations of the linewidth enhancement factor at room temperature in a selection of mid-infrared active region materials. The linewidth enhancement factor is correlated with three features of the electronic structure: conduction and valence densities of states balancing, conduction band dispersion, and judiciously placed intersubband absorption features. Calculations were performed on a 4.2 μm strained 150Å InAsSb/300Å AlInAsSb quantum well structure,[29] a 4.4 μm strained 80Å InAsSb/80Å InAsP quantum well structure,[30] a 4.0 μm 15Å InAs/25Å $Ga_{0.60}In_{0.40}Sb$/15Å InAs/39Å $Al_{0.30}Ga_{0.42}In_{0.28}As_{0.50}Sb_{0.50}$ superlattice,[14,31] and a 4.1 μm 21Å InAs/31Å $Ga_{0.75}In_{0.25}Sb$/21Å InAs/43Å AlSb superlattice.[32] Bulk $InAs_{0.91}Sb_{0.09}$ (lattice matched to GaSb) is included as a reference. Although the linewidth enhancement factor of a real device is affected by the optical cavity,[23,33] the value is dominated by the inherent linewidth enhancement factor of the active region material. Comparison of the linewidth enhancement factor of the different materials allows for the evaluation of these materials as active regions for either spectrally pure or high-power applications.

The optical properties of the materials were calculated using a superlattice **K·p** formalism with a 14 bulk band basis. This method is an extension of the eight-band **K·p** formalism that has been used previously to calculate the optical properties of a variety of mid-infrared materials.[14] Excellent agreement has been seen between a variety of theoretical calculations and experimental measurements.[34] Gain and intersubband absorption spectra were calculated for TE polarization as a function of carrier density using the highly nonparabolic band structure and momentum-dependent matrix elements. A Kramers-Krönig transformation of the change in absorption spectra for each density was performed to obtain the nonlinear change in the index of refraction. The differential gain, differential index, and linewidth enhancement factor were calculated for the transition energy corresponding to the peak of the gain spectrum.

Strictly, the Kramers-Krönig transformation should be applied over the entire energy spectrum, whereas we use a finite energy range (transition energies up to ~0.8 eV). However, calculating the *change* in index from the *change* in absorption spectrum is a very different problem than calculating the *index of refraction* from the *absorption* spectrum. The index of refraction is dominated by the magnitude of the absorption spectrum at Van Hove singularities away from zone center, but the change in absorption spectra is only non-zero where the nonequilibrium carriers are (near zone center for the direct gap materials discussed here). We can approximate the effect of using a finite energy range in our calculations by repeating the

calculations using a substantially larger energy range. From this procedure, we estimate the error introduced by the use of a finite energy-range in the calculation of the change in index spectrum at the expected lasing energy to be less than 10%.

The results of our calculations of linewidth enhancement factors are listed in Table III. In order to facilitate the comparison of different material systems, we focus on the relative differential gain spectrum. Plots of the gain, relative differential gain, and linewidth enhancement factor are shown in Fig. 11 as a function of transition energy for four of the five systems considered (the curves for system IV are similar to those of system V). The parameters are calculated for the carrier density at which the linewidth enhancement factor at the peak of the gain spectrum takes on its minimum value. By examining Fig. 11 we can track the change of behavior from system I (Fig. 11 (a)), which is a bulk system, through system II (Fig. 11(b)) and system III (Fig. 11(c)), which are quantum wells with increasing levels of confinement, to system V (Fig. 11(d)), which is a type-II superlattice with very large band offsets.

Bulk InAsSb has the largest linewidth enhancement factor of all of the systems considered. The large linewidth enhancement factor is fundamentally a consequence of the significant imbalance between the conduction and valence band densities of states. Density of states mismatch leads to a large linewidth enhancement factor through two processes. First, significant imbalance in the densities of states reduces the differential gain near the band edge by decreasing the penetration of the hole Fermi energy into the valence band. Second, density of states imbalance broadens the differential gain spectrum. The peak of the differential gain spectrum will occur roughly at a transition energy of $E_g + E_{Fc}$, where E_g is the band gap and E_{Fc} is the conduction band Fermi energy measured from the conduction band minima.[22] When the density of states of the valence band is significantly larger than that of the conduction band, E_{Fc} becomes increasingly large.

The imbalance between the conduction and valence densities of states can be quantified using the ratio of the valence and conduction band-edge Fermi occupation functions at a density where the sum of the Fermi functions is 1.0 (which is a minimal condition for gain).[35] This quantity is a measure of the contribution to inversion from the valence and conduction bands. A system with ideal balancing of the densities of states would have a ratio of 1.0. Using this measure, the density of states imbalance for bulk InAsSb is 25.7. Calculated values are shown in Table III for all of the materials.

	System	E_g (μm)	α_{lwe} at γ_{net}^{max}	α_{lwe} $\gamma_{net} > 50cm^{-1}$	ρ_v / ρ_c	$d\gamma / dN$ (x10^{-16} cm^2)	ΔE_{CB} (meV)
	BULK MATERIALS						
I	$InAs_{0.91}Sb_{0.09}$	4.2	6.5	1.8	25.7	3.5	bulk
	TYPE-I QUANTUM WELLS						
II	InAsSb / AlInAsSb	4.2	5.4	2.0	9.9	4.8	0.3
III	InAsSb / InAsP	4.4	2.5	1.7	7.6	13.9	21.2
	TYPE-II SUPERLATTICES						
IV	InAs / GaInSb / InAs / AlSb	4.1	1.1	0.4	2.0	33.6	2.5
V	InAs / GaInSb / InAs / AlGaInAsSb	4.0	0.9	0.3	2.3	27.0	36.2

Table III: Calculated values of the linewidth enhancement factor for five mid-infrared active region materials at room temperature. E_g is the band gap, α_{lwe} is the linewidth enhancement factor, ρ_v / ρ_c is a measure of the ratio of the valence to conduction band densities of states, $d\gamma_{net} / dN$ is the differential gain at the peak of the gain spectrum, and ΔE_{CB} is the miniband width of the lowest conduction subband.

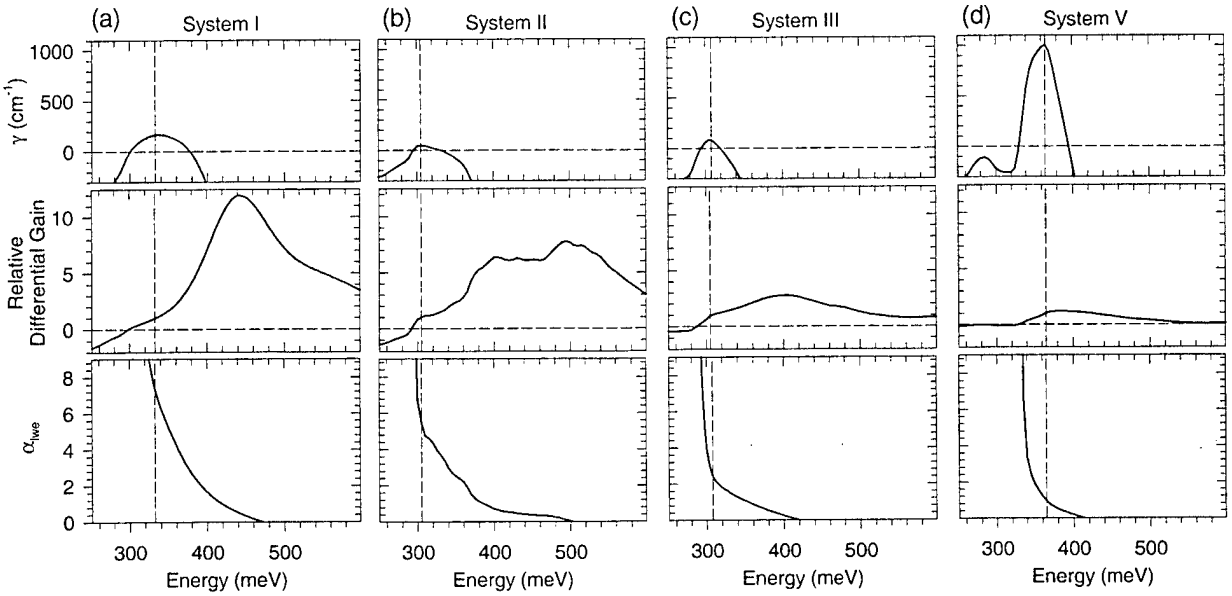

Figure 11. Gain, relative differential gain, and linewidth enhancement factor as a function of transition energy for (a) system I, bulk $InAs_{0.91}Sb_{0.09}$, (b) system II, an InAsSb/AlInAsSb quantum well, (c) system III, an InAsSb/InAsP quantum well, and (d) system V, a type-II superlattice. The curves for each system are calculated for the carrier density at which the linewidth enhancement factor at the peak of the gain spectrum is a minimum. The vertical dashed lines are the energy of the peak of the gain spectrum.

System II is a compressively strained quantum well with small band offsets for both the electrons (90 meV) and holes (72 meV). The quantum confinement and compressive strain reduce the density of states imbalance to 9.9 by splitting the heavy and light valence subbands. However, the band offsets are not large enough to significantly improve the differential gain, so the linewidth enhancement factor is only slightly smaller than that of bulk InAsSb.

System III is a multiple quantum well structure with a narrower well, twice the electron and hole confinement, and twice the compressive strain of system II. Because of this, the differential gain at the peak of the gain spectrum (13.9×10^{-16} cm^2) is significantly larger than either systems I or II.

One of the main advantages of the type-II InAs/GaInSb material system is the large band offsets (>0.5 eV) possible in both the conduction and valence bands. In addition, because the valence band well is typically very thin (~20 – 30 Å), it is possible to incorporate much larger strains (~2.5%) than in the thicker type-I quantum wells. The additional strain and quantum confinement makes it possible to design materials with density of states mismatch that are more than a factor of three smaller than either of the type-I quantum wells. It is this same improvement in the balancing of the density of states that makes the type-II superlattices attractive for low threshold operation.[14] For system V, the differential gain (27×10^{-16} cm^2) is more than twice that of system III. In addition, the differential gain spectrum is significantly narrower than the bulk and type-I systems.

Within each type of structure (type-I or type-II), those with larger conduction band dispersion (listed in Table III) have smaller linewidth enhancement factors. The presence of dispersion in the conduction band shifts the peak of the gain spectrum (and hence, the lasing energy) from the band edge to an energy roughly the miniband width above the band edge. The region of positive differential gain between the band edge and the shifted gain spectrum peak reduces the density-dependence of the index of refraction and the value of the linewidth enhancement factor at the peak of the gain spectrum. The impact of dispersion in the conduction band on the threshold carrier density of a laser is not substantial if the miniband width is comparable to the thermal energy (k_BT).

The advantage of conduction band dispersion can be seen in a comparison of systems IV and V. Because system V uses a quinternary alloy as the superlattice barrier layer rather than

AlSb, there is a slight coupling between adjacent periods of the superlattice, which results in 36 meV of dispersion in the conduction band. The impact on the gain, relative differential gain spectrum, and the linewidth enhancement factor can be seen in Fig 12 as a function of energy from the peak of the gain spectrum. The gain spectrum of system V (solid line) is significantly broader than that of system IV (dashed line) because of the dispersion in the conduction band. The broadening of the gain spectrum at energies below the peak of the gain spectrum results in a broadening of the relative differential gain spectrum. The region of positive differential gain below the peak gain energy reduces the resulting linewidth enhancement factor, in spite of the fact that the differential gain spectrum for system V is broader at energies above the peak gain.

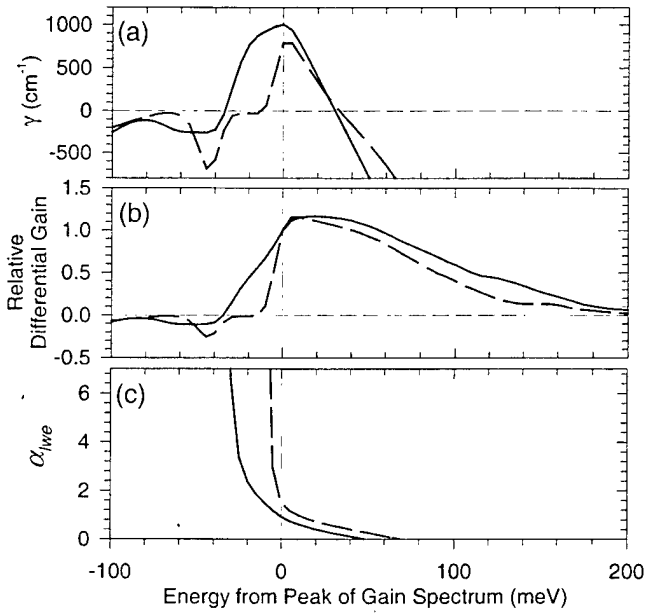

Figure 12. (a) Gain, (b) relative differential gain, and (c) linewidth enhancement factor spectra for systems IV (dashed line) and V (solid line) as a function of the energy from the peak of the gain spectrum (vertical dashed line).

An additional optimization can be used to reduce the linewidth enhancement factor in the type-II superlattices. Intersubband absorption features in these superlattices are relatively sharp due to the highly structured nature of the valence subbands. It is possible to adjust the energy of the subbands by modifying the layer thicknesses and alloy compositions in such a way as to place a large absorptive feature above the peak of the gain spectrum. The presence of this large density-dependent absorption feature just above the lasing energy will reduce the density-dependence of the index of refraction at the lasing energy without reducing the differential gain.

Thus the linewidth enhancement factor will be reduced. An example of this is shown in Fig. 13 for two 4.5 μm type-II superlattices. The placement of the resonance at 305 meV in one structure rather than 255 meV in the other leads to a 34% reduction of the linewidth enhancement factor at the peak of the gain spectrum. For both systems, the curves shown represent the density at which the linewidth enhancement factor is a minimum. A similar use of intersubband absorption resonances has been used to tailor the index of refraction in a material for the purpose of phase matching.[36]

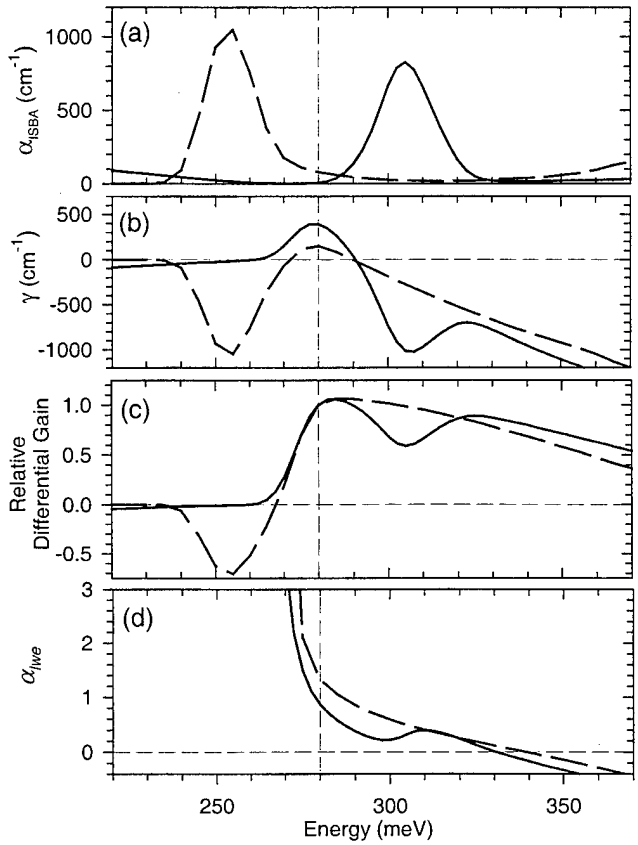

Figure 13. Placement of intersubband absorption features can be used to reduce the linewidth enhancement factor in type-II superlattices. (a) Intersubband absorption, (b) gain, and (c) relative differential gain, and (d) linewidth enhancement factor spectra for an optimized (solid) and a deoptimized (dashed) four-layer superlattice. The optimized superlattice is 30 Å $Ga_{0.55}In_{0.45}Sb$ / 18 Å InAs / 65 Å $Al_{0.30}Ga_{0.42}In_{0.28}As_{0.50}Sb_{0.50}$; the deoptimized structure is 38 Å $Ga_{0.75}In_{0.25}Sb$ / 20 Å InAs / 65 Å $Al_{0.30}Ga_{0.42}In_{0.28}As_{0.50}Sb_{0.50}$. The vertical dashed line is the energy of the peak of the gain spectrum for both structures.

The discussion to this point has focused on the linewidth enhancement factor at the peak of the gain spectrum. We can estimate the minimum linewidth enhancement factor that can be

obtained through detuning of the lasing frequency with a DFB structure by calculating the minimum linewidth enhancement factor over the energy range where the gain is greater than some minimum value. The results for a minimum gain value of 50 cm^{-1} are shown as a function of carrier density in Fig. 14 for systems I, II, and V; the minimum value for each of these curves is listed in Table III. It is possible to obtain linewidth enhancement values as low as 0.3 with the type-II superlattices. This represents a very attractive value for spectrally pure or high power laser operation.

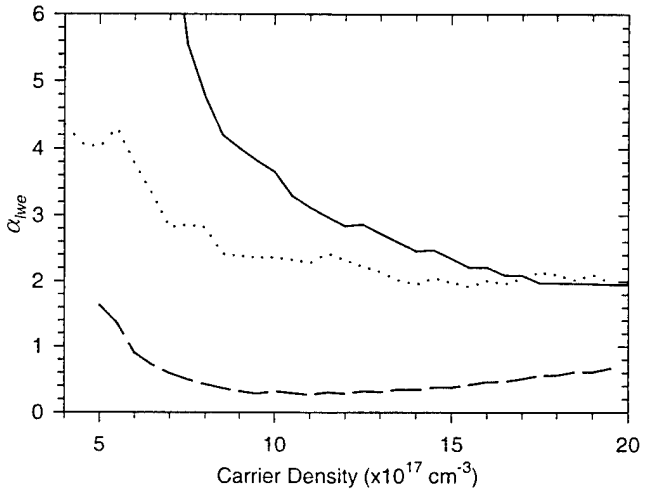

Figure 14. Minimum linewidth enhancement factor at any energy with greater than 50 cm^{-1} of gain for bulk InAsSb (system I, solid line), a type-I quantum well (system II, dashed line), and a type-II superlattice (system V, dash-dot line). These curves represent an estimate of the minimum linewidth enhancement factor attainable with a DFB structure.

Linewidth Enhancement Factor - Measurement

The tunability of the ultrafast OPO can be used to measure spectra of the pump induced change in absorption,[9, 10] of MWIR laser materials, and from this we can experimentally estimate the linewidth enhancement factor. We have applied this to studies of an optimized 4-μm-band-gap, 4-layer BGSL. The optimization of the optical properties of this structure is evident from the calculated gain and intersubband absorption, shown over a broad spectral range in Fig. 15. This illustrates that large gain can be achieved at low carrier densities and that the intersubband absorption is spectrally isolated from the band-edge gain. The overall agreement between the measured and calculated change in absorption is shown in Fig. 16 and indicates that intersubband absorption indeed does not significantly affect the measured results within this spectral region.

This ability to evaluate intersubband absorption is crucial to identifying and ultimately suppressing internal loss, a process critical for high-power laser operation.

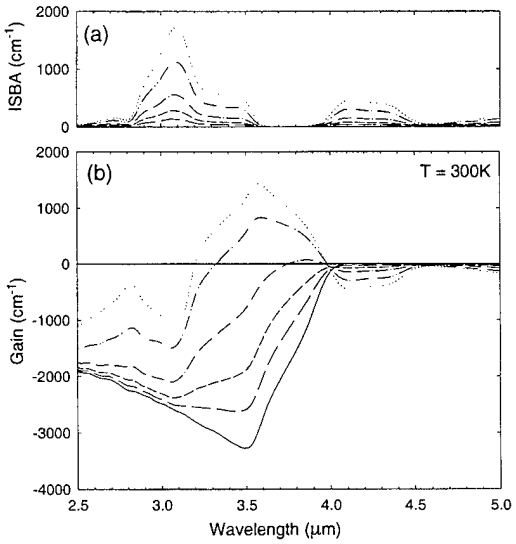

Figure 15. (a) Intersubband absorption (ISBA) spectra and (b) gain spectra determined theoretically for the four-layer superlattice shown for the following carrier densities: 0 (solid), 1.3 (long dashed), 2.7 (short dashed), 5.3 (dash-dot), 10.6 (dash-dot-dot), and 15.9 (dotted) x 10^{17} cm^{-3}.

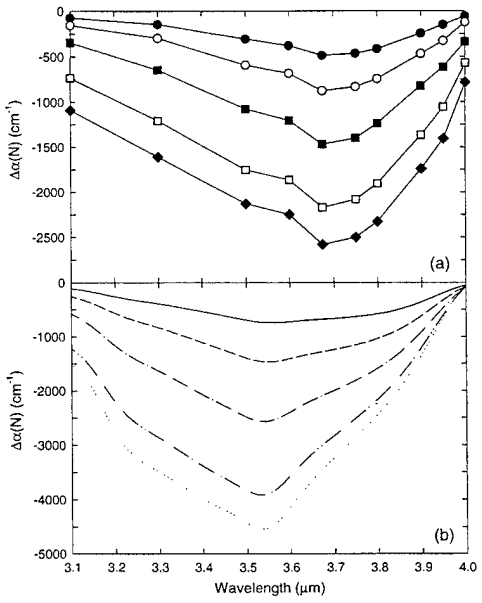

Figure 16. (a) Experimental change in absorption spectra for carrier densities of: 1.3 (filled circles), 2.7 (open circles), 5.3 (filled squares), 10.6 (open squares), and 15.9 (filled diamonds) x 10^{17} cm^{-3} and (b) theoretical carrier-induced change in absorption spectra for the following carrier densities: 1.3 (solid), 2.7 (dashed), 5.3 (dash-dot), 10.6 (dash-dot-dot), and 15.9 (dotted) x 10^{17} cm^{-3}.

Comparison of measured and theoretical spectra shows quite reasonable agreement, given the complexity of both the structure and the measurements. Still, the calculated maximum change in absorption is roughly twice the measured value. This means that the measured differential gain will also be half the calculated value, which in turn increases the predicted threshold current density by a factor of two. This discrepancy, which is also seen in the BGQW differential gain spectra but not in spectra from the earlier BGSL MQWs.[9]

The differential absorption spectra is directly related to the net material differential gain spectra. A Kramers-Kronig transformation of these spectra yields spectra of the differential index of refraction, as shown in Fig. 17. These results can be used to compute the material linewidth enhancement (LWE) factor for the SL, as shown in Fig. 18. We find that the measured LWE factor is extremely small (~1) in these structures at wavelengths and densities appropriate for lasing, an attractive feature for high power or narrow line operation.

Development and Application of Novel Ultrafast Optical Techniques

We have adapted our photoluminescence upconversion technique to provide time-resolved density-dependent absorption spectra over a broader range than can be accessed by our OPO. This approach, which is based on femtosecond upconversion of incoherent blackbody radiation transmitted through an MWIR structure, is illustrated schematically in Fig. 19. Again, measurements have been conducted on the same 4-layer MWIR BGSL, and results are shown in Fig. 20 along with a theoretical spectrum based on the 14-band **K•p** model and momentum dependent matrix elements. The theoretical differential transmission has been scaled by roughly a factor of 2 to account for the difference in measured and calculated absolute magnitudes mentioned earlier and shifted slightly to account for small discrepancies between measured and calculated band gaps. The results show that excellent agreement in the overall shapes and width of the lowest energy transition (heavy-hole 1 to conduction band 1) but a 40 meV error in the theoretical location of the light-hole 1 to conduction band 1 transition. The details of the valence subband structure are extremely important to final-state optimization strategies related to suppression of Auger recombination and intersubband absorption in this and similar laser structures.

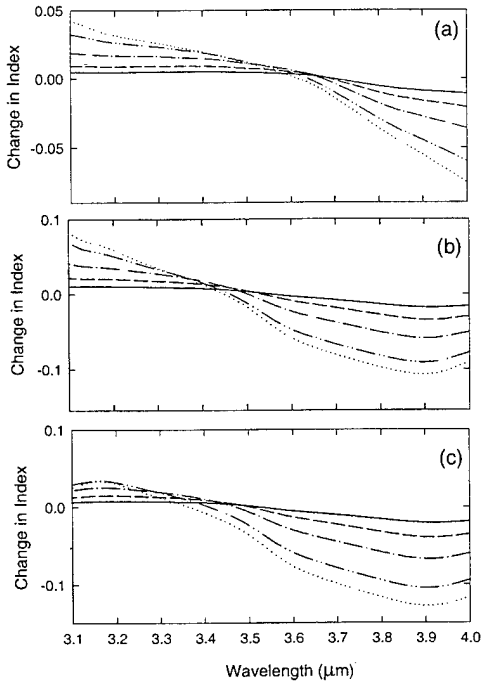

Figure 17. Carrier-induced change in refractive index, for the densities: 1.3 (solid), 2.7 (dashed), 5.3 (dash-dot), 10.6 (dash-dot-dot), and 15.9 (dotted) x 10^{17} cm^{-3}, obtain from (a) a smooth fit to $\Delta\alpha(N)$, (b) the theoretical $\Delta\alpha(N)$ from 3.1 - 4.0 μm, (c) the full theoretically determined $\Delta\alpha(N)$ from 1.24 - 23.3 μm.

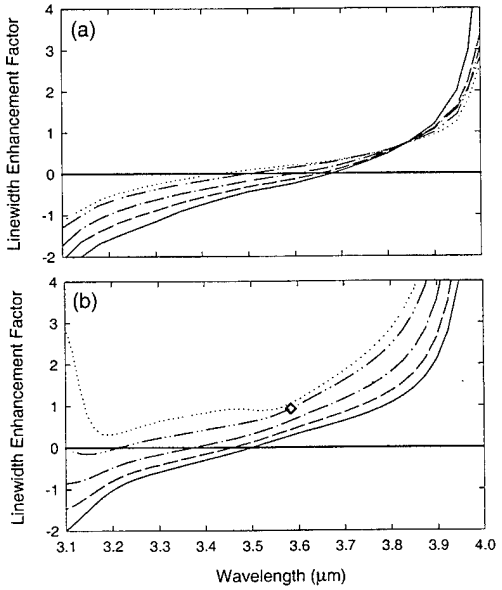

Figure 18. The experimental (a) and theoretical (b) linewidth enhancement factors for the carrier densities: 1.3 (solid), 2.7 (dashed), 5.3 (dash-dot), 10.6 (dash-dot-dot), and 15.9 (dotted) x 10^{17} cm^{-3}. The linewidth enhancement factor and wavelength of the peak theoretical gain at threshold (1.06 x 10^{-18} cm^{-3}) is indicated by the open diamond.

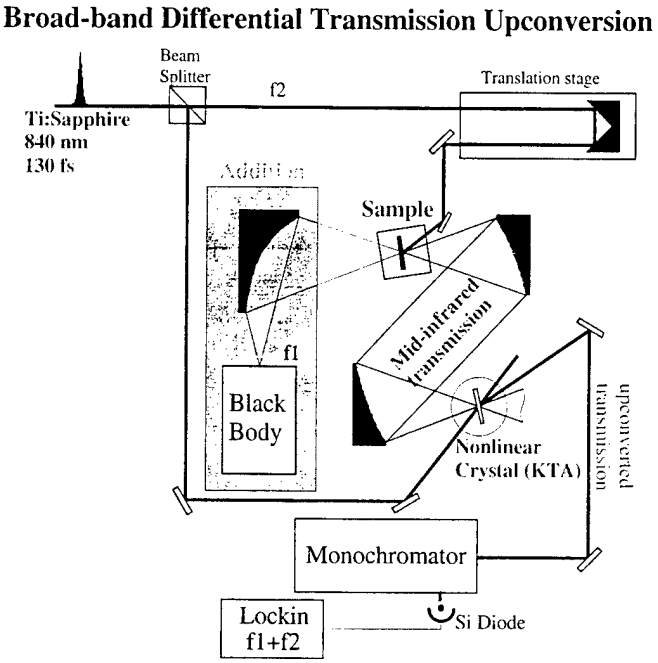

Figure 19. Schematic diagram of broad-band time-resolved transmission measurement based on the subpicosecond upconversion of continuous blackbody radiation.

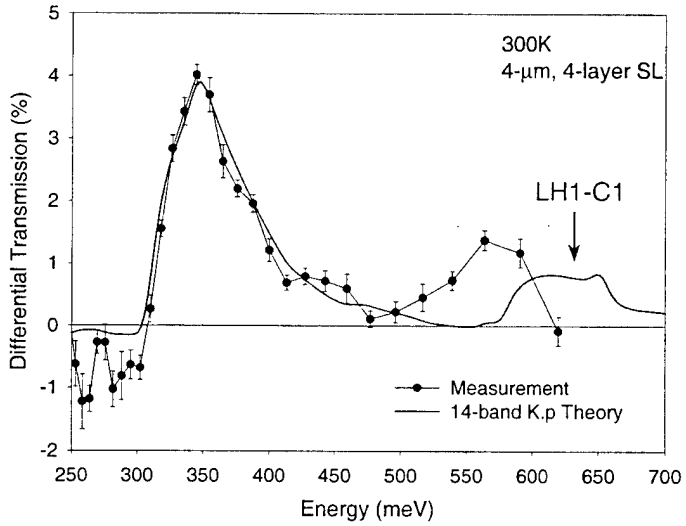

Figure 20. Time-resolved transmission spectrum of a 4-μm, 4-layer BGSL obtained using a blackbody upconversion technique.

Carrier Recombination

Validity of Theoretical Models for Auger Recombination

A significant goal of electronic structure engineer of MWIR materials is the suppression of Auger recombination, both through band edge optimizations and final state optimization. To this end, we have applied our time-resolved spectroscopic systems to measurements of Auger recombination in a variety of antimonide microstructures. [11, 31, 37] The theoretical predictions of reduced Auger recombination were experimentally verified by performing pump/probe measurements on the 4-μm, 4-layer BGSL. Results are shown in the lower left panel of Fig. 21. We find that the Auger rate is suppressed by roughly a factor of four relative to that expected for Type-I structures of comparable band gap or unoptimized Type-II structures, such as the early-generation BGSL MQWs. Theoretical results are compared to the data in Fig. 21 (open diamonds). Using no adjustable parameters, the 14-band **K•p** model provides excellent agreement with experimental Auger rates. The theoretical results illustrate the importance of SL Umklapp scattering on the Auger recombination. Neglect of Umklapp processes reduces the theoretical values by a factor of approximately 2.5, thus yielding much poorer agreement. We have also found that the temperature dependence of the Auger rate is well predicted by theory.[11]

The 14-band **K•p** model has proven to be extremely accurate at predicting Auger recombination in a wide variety of structures. This is also illustrated in Fig. 21, which shows a comparison between theory and measured results for four different samples from four different growers. The samples include both bulk and microstructures with band gaps in both the MWIR and LWIR. The agreement between theory and experiment is remarkable, indicating that the theoretical band structure can be used with confidence as a guide for laser design.

Auger Recombination in the 4-Layer BGSL

The temperature dependence of the Auger process is particularly relevant to diode laser design, since lasers designed for Auger suppression at one temperature may not be optimized at another[38] and the temperature dependence in MWIR quantum wells and superlattices may not display the trends that one might anticipate from simple models.[39] It is well known that in near-infrared-band-gap bulk materials the Auger rate increases strongly with increasing temperature.[40]

The temperature dependence in near-infrared band-gap *quantum wells*, however, has been observed to be significantly reduced, leading some investigators to conclude that phonon-assisted Auger recombination dominates in these structures.[40, 41] Others have concluded that band-to-band Auger recombination still dominates,[42] but electrostatic band profile deformation influences the band edge populations in a manner that decreases the temperature dependence of the Auger rate.

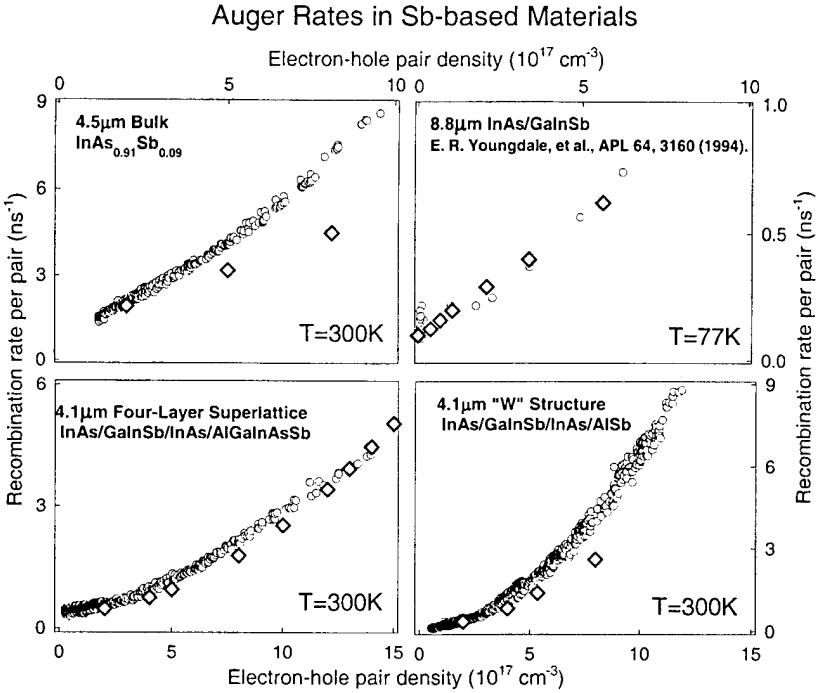

Figure 21. Measured and calculated Auger rates for the four indicated structures.

The temperature dependence of Auger recombination in some *bulk* MWIR III-V semiconductors is more complicated than in near-IR materials. This is a consequence of the proximity of the spin-orbit split-off band energy, Δ, to that of the fundamental gap, E_g, in narrow-band-gap semiconductors, such as InAs and related alloys. The split-off band can thereby provide resonant states for hole-hole (CHHS) Auger processes. Since the temperature dependence of E_g and Δ are generally different, the Auger resonance energy may move relative to the band-gap energy, and therefore the Auger rate, may increase or decrease with temperature.[43] Similar arguments can be made with respect to subbands in MQWs and minibands in superlattices, potentially leading to unexpected temperature dependence to the recombination in such structures. For example, the Auger rate in a 275-meV-band-gap

InAs / $Ga_{0.69}In_{0.31}Sb$ / InAs / AlSb type II MQW was found to increase with temperature modestly in a monotonic manner.[44] On the other hand, the Auger rate was found[45] to saturate with temperature in a 400 meV InAs / GaSb / $Ga_{0.75}In_{0.25}Sb$ / GaSb superlattice designed with a valence band Auger resonance in the middle of a minigap. Furthermore, the Auger coefficient was found to actually decrease with temperature above ~ 180 K in a similar superlattice designed with a heavy-hole-1 to heavy-hole-3 Auger resonance.[46] Such widely varying results indicate the importance of understanding the temperature dependence of the Auger process in structures designed for MWIR lasers.

Time-resolved PL upconversion, was used to investigate the density and temperature dependence of the recombination in the 4-μm-band-gap 4-layer BGSL. PL decay curves for lattice temperatures of 50, 100, 150, 175, 200, 230, 260 and 300 K were measured for a range of initial carrier densities. Representative curves are shown in Fig. 22 for four lattice temperatures. The decay rate of the PL clearly increases both with increasing lattice temperature and increasing initial carrier density. We attribute the fast decay occurring within a few hundred picoseconds at high carrier densities to Auger recombination and the slower feature at longer delays to Shockley-Read-Hall recombination. These assertions are justified in the analysis discussed below.

The initial carrier densities, which are crucial in determining Auger rates, were calibrated by comparing selected experimental time-resolved PL spectra with those calculated based on the calculated temperature-dependent band structures shown in Fig 23. For these measurements, the time delay between the pulse used to excite the sample and that used for the upconversion process was fixed at 10 ps and the entire PL spectrum was measured. The carrier temperature was extracted from the high energy tail of the spectrum and used in calculations of the PL for a range of carrier densities. As illustrated in Fig. 24, the calculated PL spectra were then compared to the experimental spectra to yield the carrier density. Note that these results are plotted on a semi-log scale to illustrate the exponential energy dependence of the tail of the spectrum. The slope of this high energy tail is primarily indicative of the carrier temperature, while for a reasonably cool distribution the overall width of the spectrum is largely controlled by the carrier density as a consequence of band filling.

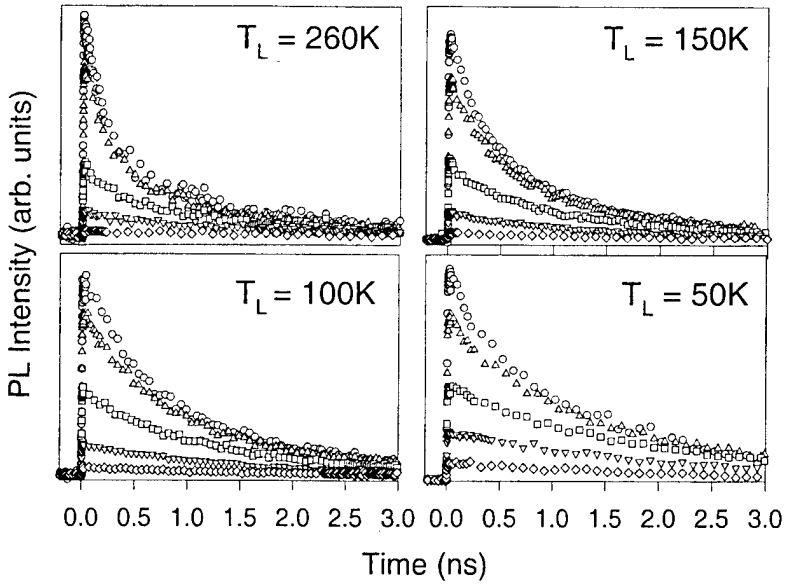

Figure 22. Time-resolved photoluminescence measured near the band gap energy for lattice temperatures of 50, 100, 150, and 260K and initial carrier densities of (from the top) 1.7 x 10^{18}, 1.1 x 10^{18}, 5.7 x 10^{17}, 2.8 x 10^{17}, and 1.4 x 10^{17} cm^{-3}.

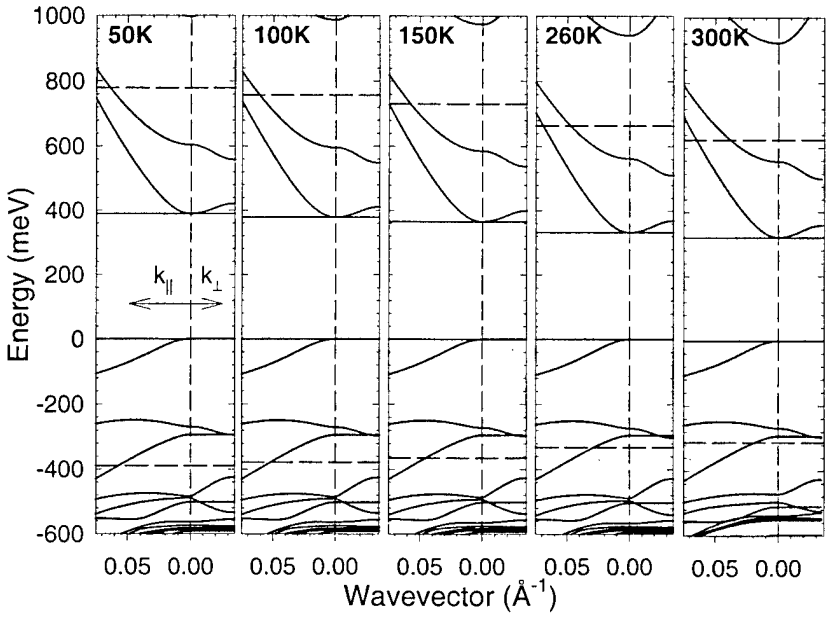

Figure 23. Temperature-dependence of the band structure for the 4-μm-band-gap (300K) 4-layer BGSL.

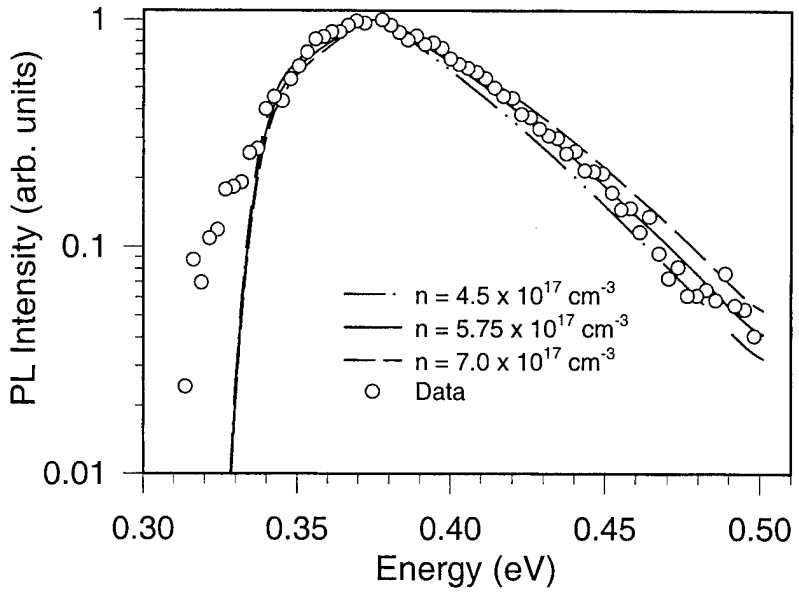

Figure 24. Plot of calculated (lines) and measured (circles) time-resolved (10 ps after excitation) photoluminescence for an excitation fluence of 8 μJ/cm^2, a lattice temperature of 260K, and a carrier temperature of 300K. Calculated PL for carrier densities of 4.5 x 10^{17}(dash-dot-dotted line), 5.75 x 10^{17}(solid line), and 7.0 x 10^{17} cm^{-3} (dashed line) are indicated.

In fitting the spectrum, we fix the band gap energy at the low-density value obtained from CW PL (band gap renormalization is insignificant at the densities of interest in this low-mass semiconductor), use the carrier temperature obtained from the high energy portion of the spectrum, and then adjust only the carrier density to obtain a best fit to the data. The PL observed below the band edge is present at all densities indicating that it is a consequence of band tailing. These data are ignored in the fits. We assume in the calculations that within 10ps after optical excitation the initially hot carriers diffuse across the thin superlattice and are uniformly distributed in the growth direction at the time of the measurement. Since the experimental arrangement ensures that only the emission from the central portion of the excited region of the sample is upconverted, transverse variations in the density are ignored. Shown in Fig. 24 are theoretical results for three values of the carrier density, illustrating that this procedure is sensitive to variations in density of approximately +/-20%. This process was repeated for various temperatures and excitation conditions. We conclude from this process and from knowledge of our optical excitation intensity that, over the range of our experimental conditions, essentially all of the incident photons transmitted through the semiconductor surface

produce carriers that are confined to the superlattice, nominally independent of lattice temperature and excitation level. Hence, for this structure, the initial carrier density is readily determined from the incident photon flux.

The data in Fig. 22 are converted to density dependent rates, $R(n)$, using

$$R(n) = \frac{1}{n}\frac{\partial n}{\partial t} = \frac{1}{n}\frac{\partial n}{\partial I_{PL}}\frac{\partial I_{PL}}{\partial t}, \qquad (5)$$

where I_{PL} is the intensity of the PL and the derivatives are readily obtained from Fig. 22. Specifically, $\partial I_{PL}/\partial t$ is obtained directly from Fig. 22 and $\partial I_{PL}/\partial n$ is obtained from a functional fit to the peak PL signals measured at each excitation level. This procedure is illustrated in Fig. 25, where we show the fit and the normalized measured peak PL signal as a function of carrier density for the 260K data. $R(n)$ is interpreted as the sum of radiative and nonradiative rates. Photon reabsorption[47] is not considered here because of the small excitation beam size (50μm), thin active region (0.375μm), low band edge absorption coefficient (approximately 2000cm^{-1}), and relatively small radiative rate (never larger than 10% of the total recombination rate). To obtain the nonradiative for each density, we subtract from $R(n)$ the calculated radiative rate, a quantity that is readily determined from the band structure and matrix elements and is essentially insignificant relative to Shockley-Read-Hall and Auger recombination in this structure.

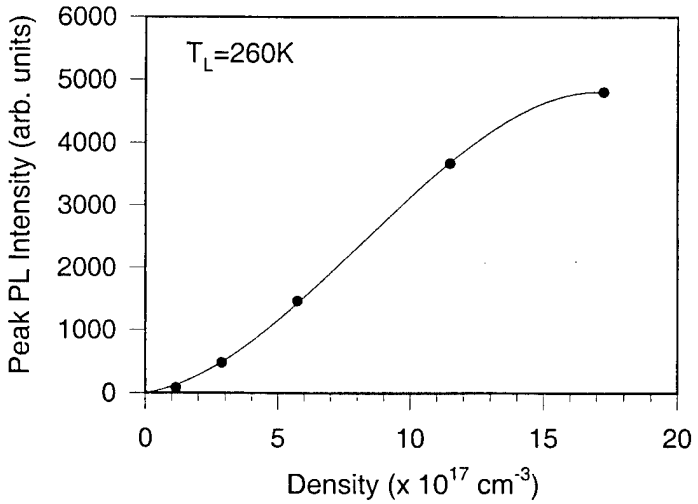

Figure 25. Peak PL intensity as a function of carrier density for a lattice temperature of 260K. The curve represents a smooth functional fit to the data from which the partial derivative $\partial I_{PL}/\partial n$ is obtained and used in the evaluation of the recombination rate R(n).

This procedure yields the nonradiative rates as a function of density as shown in Fig. 26 for the same lattice temperatures and initial carrier densities as depicted in Fig.22. Note that the data shown in Fig. 26 originate, in essence, entirely from experiment, with theory invoked only to account for the minor effect of radiative recombination and to calibrate the initial carrier density. The intercepts in these plots yield the Shockley-Read-Hall rates, which correspond to lifetimes in all cases of > 2 ns. This value is within the 2-4 ns range typical of antimonide structures grown in this MBE system (Perkin-Elmer 430P) and is within a factor of < 5 of the best MBE-grown antimonide structures studied in our laboratory. The specific origin of this density-independent recombination is not known, but may be associated with defects in the quinternary layers and/or interface states.

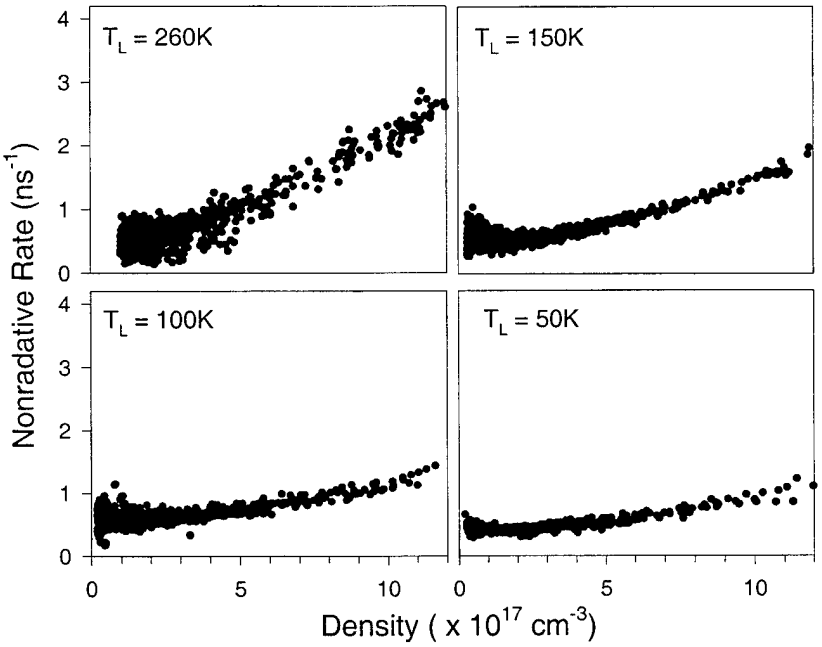

Figure 26. Nonradiative recombination rates at lattice temperatures of 50, 100, 150, and 260 K obtained from the data in Fig. 4 using density calibrations such as that shown in Fig. 5 and the approach described in the text.

Since the radiative rate has been removed from the results of Fig. 26, deviations from a zero slope are a consequence of Auger recombination. The data clearly illustrate an Auger rate that increases uniformly with both increasing carrier density and increasing temperature. We find that the density dependence of the Auger rate is sub-quadratic with carrier density,[48] a consequence of degeneracy of both the conduction and valence bands over much of the density

range of interest. The effects of degeneracy have been confirmed through detailed investigations of the density dependence of the recombination. The temperature dependence of the Auger process is seen more clearly in Fig. 27, where we plot the Auger rate as a function of lattice temperature for several different carrier densities.

The calculated direct band-to-band Auger rates are also shown in Fig. 27. These were obtained from Fermi-Golden-Rule calculations based on the nonparabolic band structure with momentum dependent matrix elements. Transition matrix elements are evaluated using a statically screened Coulomb interaction and first-order **K·p** perturbation theory for the wavefunction overlaps. The calculations are similar to those reported previously[49] but modified to include Umklapp processes in the growth direction. This *intrinsic* phenomenon characterizes scattering processes that involve a reciprocal lattice vector.[50] While these processes have little impact on Auger recombination in bulk materials, they can play a significant role in superlattices. Zone folding in such structures greatly reduces the Brillouin zone width in the growth direction (by more than an order of magnitude in our superlattice) making Umklapp processes more probable.

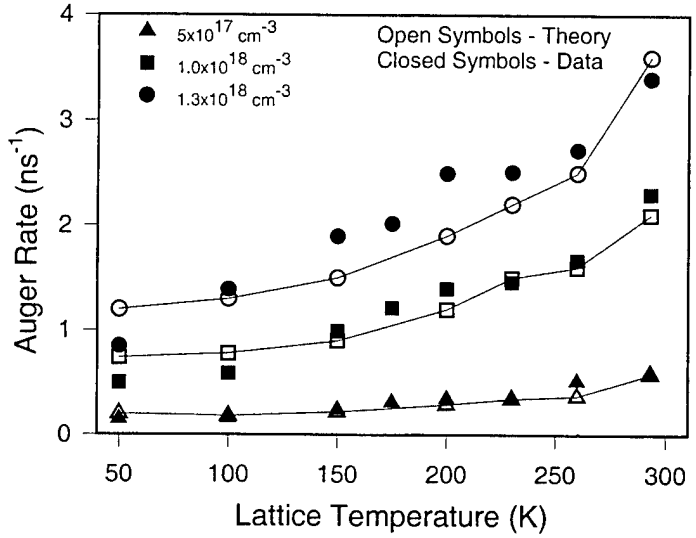

Figure 27. Measured (filled symbols) and calculated (open connected symbols) Auger rates as a function of temperature for initial densities of 5 x 10^{17} (triangles), 10 x 10^{17} (squares), and 13 x 10^{17} cm^{-3} (circles).

Calculations indicate that these processes contribute approximately half of the total Auger rate in this structure. Umklapp processes involving a reciprocal lattice vector larger than 5(2π/D), where D is the superlattice period of 94 Å, are negligible. We find that the theory

successfully predicts both the density dependence and the temperature dependence of the Auger process as well as the absolute rate. The latter, however, must be placed in context with the roughly 10% systematic and random error in the data and the 20% uncertainty in carrier density.

Auger Recombination in the BGQW

More recently, we have measured Auger recombination in the new BGQW structure. The results are shown in Fig. 28 for a 3.5 μm BGQW, along with the results for the 4-μm, 4-layer BGSL. (Note that both structures are designed for 300K laser emission at 3.5 μm. Due to growth direction energy dispersion, the superlattice will lase at an energy somewhat above the band edge, whereas the quantum well will lase very near the band edge.) We measure an Auger recombination rate in the BGQW that, at the density that maximizes the threshold figure of merit, is a factor of 2.7 smaller than in the 4-layer SL.

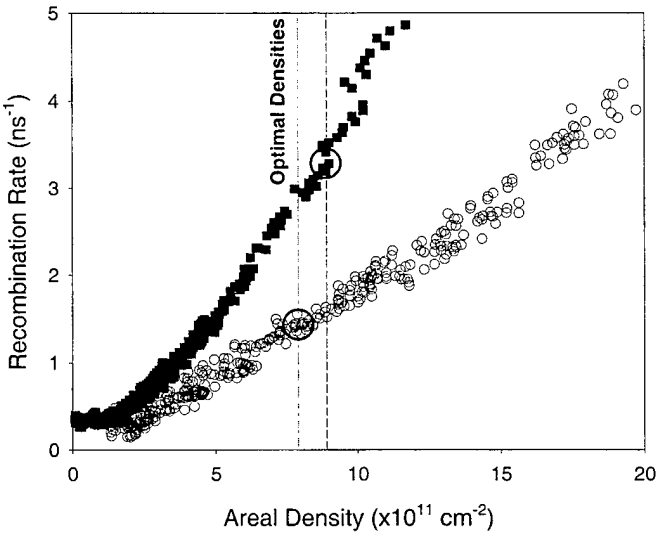

Figure 28. Measured recombination rate as a function of areal carrier density for the 4-layer superlattice (filled squares) and the BGQW (open circles). Also indicated are the densities that maximize the threshold figure of merit.

Although theory and experiment agree well for the 4-layer structure (Figs. 21 and 27), a similar comparison for the BGQW is significantly less satisfying. At the optimal density, the measured Auger lifetime is 940 ps compared to a calculated value of 35 ns. The large discrepancy is surprising given our prior success with predicting Auger rates. However, as indicated in Fig. 7, the Auger rate in the BGQW is expected to depend strongly on the nature of the final states for the Auger process. Hence, errors in either the theoretical band structure due to

uncertainties in input parameters or in the growth of the structure could lead to large differences in measured and calculated rates. Measurements on additional structures will be required to provide a definitive indication of the source of the discrepancy.

Carrier Transport and Capture

Transient Grating Measurements of In-Plane Transport

Carrier transport properties, both in the growth plane (in-plane transport) and in the growth direction (vertical transport), can significantly impact the performance of lasers and detectors. Transport measurements in the superlattices of interest on this program may provide an indicator of interface disorder, a characteristic of these noncommon-anion structures that is likely to affect device performance. Magneto-transport studies have been used to measure in-plane mobilities in such superlattices grown lattice-mismatched on semi-insulating GaAs substrates.[51, 52, 53] However, such measurements are impractical for structures grown on GaSb, since semi-insulating GaSb is not readily available. On the other hand most device interest related to these superlattices or quantum wells involves strain-balanced growth on GaSb substrates. Thus the direct measurement of transport in such structures is highly relevant to device characterization and optimization.

An alternative approach to in-plane transport measurements is based on all-optical, ultrafast, transient grating techniques.[54] These measurements rely on the interference within the semiconductor of two intense excitation pulses tuned above the band gap energy. This interference creates a modulation in carrier density, which results in a modulation of the refractive index and absorption spectra of the semiconductor. This creates a mixed amplitude-phase grating from which a third weaker probe pulse can diffract. The probe may be either at the same wavelength (degenerate) as the excitation pulses or at a different wavelength (non-degenerate). However, since the nonlinear response that gives rise to the diffraction is usually associated with thermalized and cool carriers, the diffraction efficiency is most significant for probing wavelengths near the band edge. The lifetime of the grating can be determined by measuring the diffracted probe signal as a function of relative delay between the probe and excitation pulses. The decay of the photo-generated grating is governed by a combination of carrier recombination and ambipolar diffusion, which can be separated by measuring the grating

lifetime for various grating periods. (The grating period can be varied by adjusting the angle between the two excitation pulses). This technique has been applied routinely to the measurement of diffusion of semiconductors in the near-infrared spectral region[55, 56, 57, 58, 59] but not in the MWIR, in part due to the lack of appropriate ultrafast MWIR sources.

We have used MWIR photogenerated-transient-grating techniques to measure 300K in-plane ambipolar diffusion in the 4-μm-band-gap InAs/GaInSb/InAs/AlGaInAsSb 4-layer BGSL discussed elsewhere in this Report. Measurements were conducted using subpicosecond excitation from the Kerr-lens mode-locked Ti:Sapphire laser and probe pulses from the synchronously-pumped, subpicosecond, MWIR OPO. The grating develops on a ten-picosecond time scale as the initially hot carriers relax to the superlattice band edge. The subsequent decay of the grating is measured for multiple grating periods to extract a room-temperature ambipolar diffusion coefficient that is significantly larger than that measured in bulk InAsSb (provided by Dr. George Turner of MIT Lincoln Laboratory), an alloy with comparable band gap energy. From the measured in-plane diffusion coefficient and calculated in-plane masses, we estimate a carrier scattering time, which we use together with the calculated growth direction masses to estimate the vertical electron and hole mobilities.

Two 140-fs 843-nm pulses from the Ti:Sapphire laser were interfered in the superlattice, thereby creating a modulated distribution of carriers that serves as a mixed absorption and index grating. We diffract from this grating 170-fs, 3.54-μm probe pulses from the OPO. By varying the arrival time of the probe relative to the pump pulses while measuring the resulting diffracted probe power, we obtain a direct measure of the grating decay time. The probe diffraction efficiency was measured for grating periods of Λ = 5.0, 5.9, 6.7, 7.9, and 10 μm. The density dependence of the decay was examined by varying the intensity of the two pump pulses. However, due to the strong density dependence of the recombination arising from Auger processes, the analysis of such measurements is nontrivial. The density dependent recombination was measured separately using a pump-probe technique, as discussed elsewhere in this Report. For densities above approximately $3x10^{17}$ cm^{-3}, the recombination is dominated by Auger processes. The initial measurements described herein were conducted at low excitation levels with a carrier density of $1.4x10^{17}$ cm^{-3}, where density-independent Shockley-Read-Hall recombination dominates.

The 3.54-μm probe is tuned only 40 meV above the superlattice band edge, while in contrast, the Ti:sapphire pump pulses inject carriers with roughly an electron volt of excess energy. Hence, the initial carrier distribution is extremely hot, resulting in only weak blocking of states near the band edge. This provides weak diffraction immediately after excitation, but the diffraction efficiency at the probing wavelength grows as the carriers cool. This behavior is illustrated in Fig. 29 , where we show the diffraction efficiency for the first 40 ps after excitation for grating periods of 5.0, 6.7, and 10 μm. The data show that the carriers cool on a time scale of less than 10 ps. This result is consistent with separate measurements of carrier cooling using mid-infrared, time-resolved, photoluminescence upconversion.

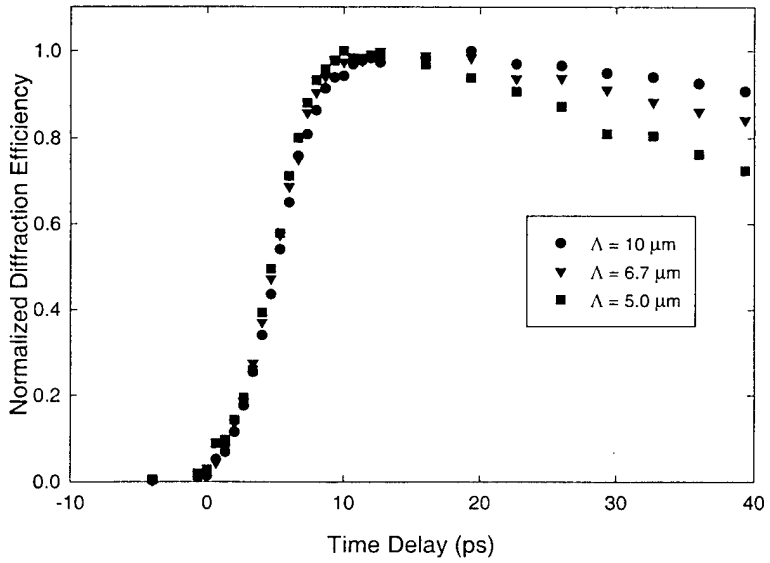

Figure 29. Normalized diffraction efficiency as a function of short time delays measured on the 4-layer BGSL sample using the transient grating measurement illustrating that the grating formation is completed within 10 ps.

Representative grating decay data are shown for much longer time delays in Fig. 30. The data clearly illustrate the increase in the decay rate with decreasing grating period suggested by the data in Fig. 2. The contribution to the decay due only to recombination, determined from the pump-probe data, is also indicated in this plot by the inverted triangles. Comparison of these data with the measured diffraction efficiency demonstrates the significance of diffusion in controlling the grating decay for these grating periods. Note that for these low-density data both the diffraction efficiency and the recombination decay exponentially with time.

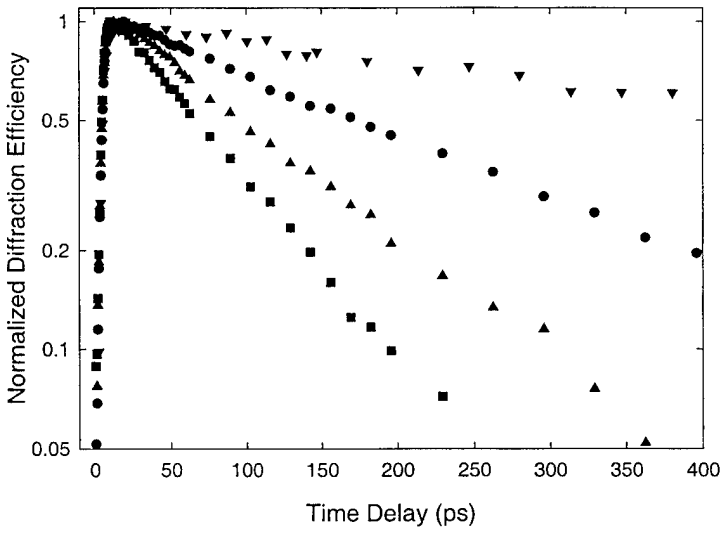

Figure 30. Decay of the diffraction efficiency as a function of grating period. The effective decay due to recombination alone is indicated by the inverted triangles.

For a sinusoidal grating and density independent recombination, the grating decay rate, Γ_G, which is half the decay rate of the diffraction efficiency, may be expressed as[54]

$$\Gamma_G = D_a\left(\frac{4\pi^2}{\Lambda^2}\right)+\frac{1}{\tau_R} \qquad (6)$$

where D_a is the ambipolar diffusion coefficient and τ_R is the Shockley-Read-Hall recombination lifetime. Under these conditions, a plot of the decay rate of the diffraction efficiency as function of $4\pi^2/\Lambda^2$ yields a straight line with a slope given by the ambipolar diffusion coefficient, while the intercept of this line with the ordinate yields the recombination rate. The result of this process, which is shown in Fig. 31, yields an ambipolar diffusion coefficient of 37±3 cm^2/s for the FLSL structure. Results of measurements performed on the bulk $InAs_{0.91}Sb_{0.09}$ epitaxial layer are also shown in Fig. 31. These data indicate a significantly lower ambipolar diffusion coefficient of 8±1 cm^2/s.

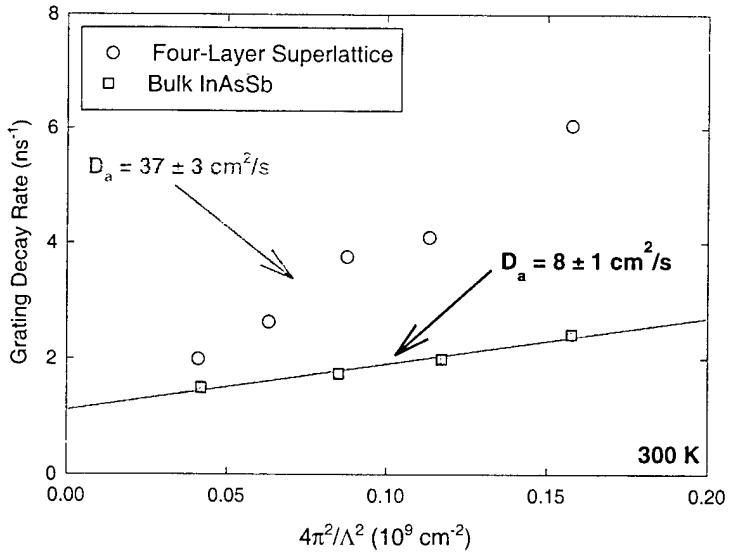

Figure 31. Plots of the diffraction efficiency decay rate for the 4-layer BGSL and bulk InAsSb (Courtesy of Dr. George Turner at MIT Lincoln Laboratory) samples used to determine the ambipolar diffusion coefficient.

We have also examined the density dependence of the in-plane diffusion in the superlattice. At high carrier densities the analysis is significantly more complicated due to density dependent recombination that leads to non-sinusoidal, density-dependent grating profiles. We have analyzed the high-density data by accounting for the measured density and temporal dependence of both the differential absorption and diffraction efficiency. By numerically modeling the decay of the diffraction grating using this information, a fit is obtained to the experimental data by using D_a as the only adjustable parameter. This analysis indicates no significant density dependence to D_a for average carrier densities up to $7x10^{17}$ cm^{-3}.

Using a linear interpolation of mobilities for the binary compounds InAs and InSb and the Einstein relation, we calculate a value of D_a = 9 cm^2/s for the lattice-matched $InAs_{0.91}Sb_{0.09}$ alloy. This is in excellent agreement with the measured result of 8 ±1 cm^2/s, thus providing confidence in both the measurements and analysis for the superlattice results.

The measured ambipolar diffusion coefficient of the 4-layer BGSL exceeds that of the InAsSb alloy by nearly a factor of five. Since in both cases the hole mass is larger than the electron mass, the ambipolar transport is expected to be more strongly influenced by holes. We therefore attribute the faster ambipolar transport in the 4-layer BGSL to the light in-plane hole mass and large heavy-hole/light-hole splitting arising from strain and quantum confinement effects in this structure.

We can compare our results with transport measurements performed elsewhere for similar structures. The diffusion coefficient that we measure in our 4-layer BGSL is larger than that calculated from 300K mobility measurements for other antimonide microstructures grown on GaAs substrates. Magneto-Hall measurements of electron and hole mobilities together with a mixed conduction analysis for an InAs/GaInSb (28 Å / 50 Å) superlattice yielded an electron mobility, μ_n, of 3500 cm^2/Vs at 300K and a hole mobility, μ_p, that was roughly an order of magnitude smaller.[53] Taking μ_p = 350 cm^2/Vs results in D_a = 16 cm^2/s, more than a factor of 2 smaller than that measured for the superlattice reported here. Meyer and coworkers have also measured a hole mobility of 300 cm^2/Vs in an InAs/GaInSb (39 Å / 11 Å) superlattice.[60] Although an electron mobility was not reported in this case, based on the hole mobility one would expect the ambipolar diffusion coefficient to be somewhat smaller than 16 cm^2/s. Similar measurements of the mobilities for an InAs/GaSb/AlGaSb (27 Å / 49 Å / 79 Å) multiconstituent MQW gave μ_n = 2700 cm^2/Vs and μ_p = 500 cm^2/Vs.[53] This yields D_a = 22 cm^2/s, a factor of 1.5 smaller than that measured in our superlattice.

The origin of the larger diffusion coefficient in our superlattice is not presently known. All of these structures have interfaces with non-common anions. It is well known that control of the interface quality in these structures is difficult, and interface disorder is known to adversely effect transport in these structures.[52] On the other hand, it is also expected that the influence of interface disorder on transport would be more significant in structures with narrower hole wells[61] (i.e., GaInSb layers), yet this trend is not evident in either the data of Meyer and co-workers or in our results relative to theirs. These findings suggest that extrinsic scattering mechanisms are likely playing an important role in the transport in these structures.

While knowledge of the in-plane carrier transport in these laser materials may be relevant to some device characteristics, it is the vertical transport that is of most significance to laser and detector performance. We can use the ambipolar diffusion measurements and the linear Boltzmann equation to extract an energy- and momentum-independent momentum relaxation time in the four-layer superlattice. This can then be used to estimate the vertical transport properties of the material. Under the simplifying assumption that the relaxation times of the electrons and holes are the same, a momentum relaxation time of 70 fs best fits the measured in-plane ambipolar diffusion coefficient for the 4-layer BGSL. This is comparable to the value of 50 fs estimated for bulk InAs. Using this relaxation time and the calculated vertical masses, we

estimate 300K vertical mobilities of 580 and 1.8 cm^2/Vs for electrons and holes. The corresponding diffusion coefficients are 15.0 and 0.05 cm^2/s. These values are significantly smaller than those for bulk InAs, particularly for holes, and are indicative of the problems associated with electrical injection in these and the W-laser structures.

Carrier Capture in a Separate Absorbing Region Laser Structure

Both the pump-probe measurements and the time-resolved PL have sufficient temporal resolution to measure carrier capture rates, i.e., the rate at which carriers from a barrier region (e.g., clad or separate-confinement region) scatter into the states associated with laser action. We have recently used time-resolved PL upconversion to examine the transfer of carriers injected into GaInAsSb separate absorbing regions into InAs/GaInSb/InAs quantum wells.[62] The structure, which was grown at MIT Lincoln Laboratories by Dr. George Turner, was designed as the active region for a 2-μm-optically-pumped laser operating near 4 μm. A schematic of the structure is shown in Fig. 32.

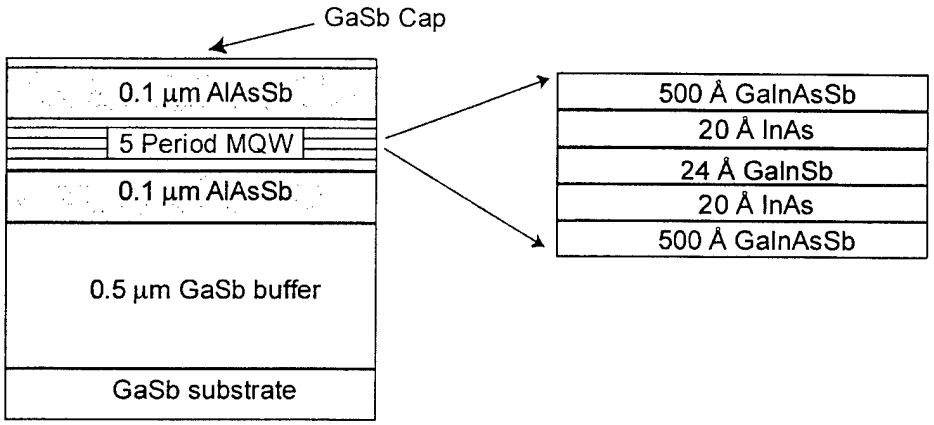

Figure 32. Schematic of the MIT separate-absorbing-region structure.

The results of measurement of emission from the absorbing (barrier) regions *and* from the well regions are shown in Fig. 33 for a lattice temperature of 80K. The PL from the barrier is found to decay with a time constant of roughly 100 ps, and the rise time of the emission from the well is well correlated with the decay of the barrier emission. This indicates that the rather rapid decay of the PL from the barrier is controlled by transfer of carriers into the wells on a time scale of approximately 100 ps. We have examined both the temperature dependence and the density dependence of the barrier and well emission. These studies indicate that the rise time of

emission in the wells decreases with increasing temperature and increasing carrier density. This suggests that both carrier-phonon and carrier-carrier scattering play a role in the filling of states near the band edge of the wells.

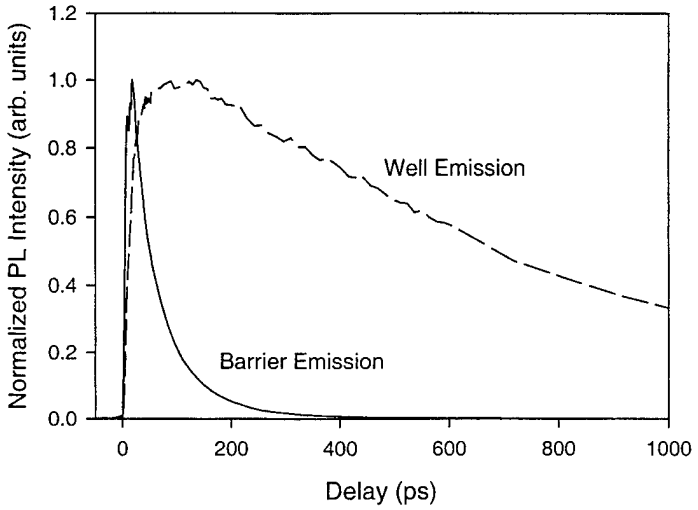

Figure 33. 80K time-resolved PL from both the quaternary barrier and from the wells in the (InAs/GaInSb/InAs)/GaInAsSb MQW. The barrier emission was measured at 2.2 μm and the well emission at 3.7 μm.

We show in Fig. 34 the measured rise time of the well emission (obtained from a single exponential fit to the data) as a function of excitation fluence for a lattice temperature of 80 and 300K. For these results, we have assumed that both electrons and holes fill the InAs/GaInSb wells in a manner described by a simple exponential rise to a constant value and that the time constants are equal for both charge species. The data clearly indicate a decrease in the rise time with increasing excitation level (carrier density) and a decrease in rise time with increasing lattice temperature. Given the band edge diagram for this structure (shown in Fig. 35), the capture rate is most likely limited by holes, which must either tunnel through or thermally hop over the InAs barriers. The latter seems highly improbable given the large hole barrier height created by the InAs. The temperature dependence of the rise time may be associated with either thermally-assisted tunneling of holes through the InAs barriers. Furthermore, one would expect that electrons would tend to be captured readily in the quantum well, leading to an effective reduction in the barrier height for holes as a consequence of Coulomb attraction. This effect should be more significant at higher carrier density, which is consistent with observation. While the precise mechanisms associated with the capture process are still under investigation, the trend

of faster capture at high carrier densities and at high temperatures is a favorable condition for optically-pumped lasers based on these structures.

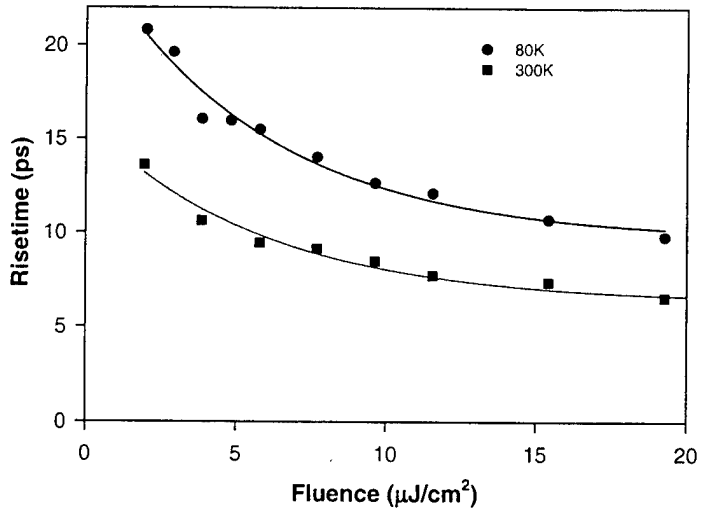

Figure 34. Summary of 77K measured photoluminescence rise times as a function of excitation fluence from the InAs/GaInSb quantum wells in the SAR optically-pumped laser structure. The solid lines are least square fits to exponential functions.

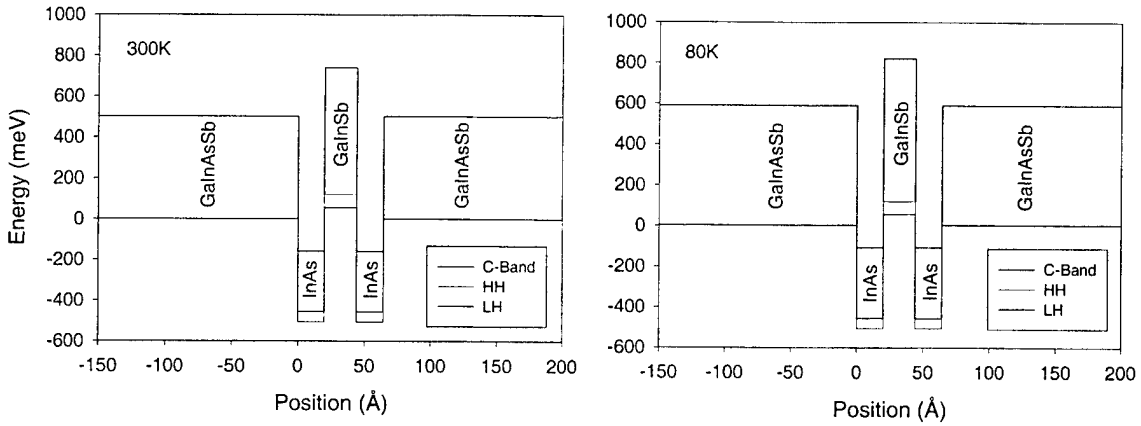

Figure 35. Band edge diagrams for the SAR InAs/GaInSb MQW at 300 and 80 K.

SUMMARY, CONCLUSIONS, AND RECOMMENDATIONS

Under this Air Force sponsored program, we have explored both theoretically and experimentally a variety of physical properties of InAs/GaInSb-based quantum structures engineered for MWIR lasers. In the process of conducting this research we have developed state-of-the-art theoretical and experimental tools that, in principle, could continue to be of value

to ongoing and future Air Force Programs. The studies demonstrate the superior properties of the InAs/GaInSb superlattice designs for MWIR lasers, indicating the possibility for large gain and differential gain, low intersubband absorption, small linewidth enhancement factors, and suppressed Auger recombination. Moreover, we have extended prior work by Korzine and Coldren to provide figures of merit for MWIR diode laser design. This, combined with measured optical and electronic properties of the antimonide structures, provides a recipe for overall diode laser design. Such designs, we conclude in agreement with prior work for wavelengths below 3 μm, must include a well-designed separate confinement region. Such considerations led us to the design of the BGQW (Fig. 6).

The BGQW structure is theoretically predicted to be vastly superior to current laser designs, including double heterostructures, W-lasers, and our own previous designs. Thus, this structure has been the focus of much of our efforts on this program. Unfortunately, as noted earlier, we have not demonstrated a working laser based on this structure. Two separate batches of lasers have been grown, processed and tested with null results. As a consequence of a limited number of growths of this structure resulting from breakdowns in our MBE machine, we have not yet been able to isolate the problems with these lasers. On the other hand, large series resistances in these structures indicate vertical transport problems, which may indicate band misalignment between either the active region and the SCR or the cladding layers and the SCR. Measurements on test structures seem to indicate that transport through the active region is problematic, although the tests are not entirely conclusive.

Due to promising properties of the BGQW but the transport problems that appear to be present, we have considered incorporating the design into an optically pumped structure while continuing to investigate the causes for the poor transport. Unfortunately, the large conduction and valence band offsets between the SCR minibands and the active region ground state sublevels that lead to strong suppression of intersubband absorption and Auger recombination lead to less than ideal conditions for optical pumping at or near 2 μm, the wavelength of choice for 3-4 μm optically-pumped lasers. Still, we predict that at room temperature a structure designed for 2-μm optical pumping should be improved relative to the current state-of-the-art. Further improvements are predicted if pumping can be done at 1.5 μm, a wavelength that allows wider band gap SCR and cladding layers, and thus larger band offsets between the SCR and the BGQW.

In spite of our unsuccessful attempts to demonstrate the BGQW diode laser, we believe that *significant* improvements in the current state-of-the-art in MWIR diode lasers will require advanced InAs/GaInSb band-structure-engineered designs. The problems that we have encountered in developing such lasers suggest that continuing studies of the fundamental material properties of the antimonide structures will be necessary to achieve this result.

REFEREED PUBLICATIONS RESULTING FROM THIS PROGRAM

1. "Mid-infrared InAs/GaInSb Separate Confinement Heterostructure Laser Diode Structures", J. T. Olesberg, M. E. Flatté, and T. C. Hasenberg, and C. H. Grein, in preparation.
2. "Ideal performance of cascade and non-cascade long-wavelength semiconductor lasers", M. E. Flatté, J. T. Olesberg, and C. H. Grein, Appl. Phys. Lett. **75**, 2020 (1999).
3. "Growth and operation tolerances for Sb-based mid-infrared lasers", C. H. Grein, M. E. Flatté, and H. Ehrenreich, J. Crystal Growth **202**, 844 (1999).
4. "Ambipolar diffusion in a type II, narrow-band-gap, antimonide superlattice," S. A. Anson, J. T. Olesberg, M. E. Flatté, T. C. Hasenberg, and T. F. Boggess, in preparation.
5. "Comparison of linewidth enhancement factors in mid-infrared active region materials," J.T. Olesberg, Michael E. Flatté, and Thomas F. Boggess, submitted to J. Appl. Phys.
6. "MBE growth and characterization of broken-gap (type II) superlattices and quantum wells for midwave-infrared laser diodes," T.C. Hasenberg, P. S. Day, E. M. Shaw, J. T. Olesberg, C. Yu, Thomas F. Boggess, and M. E. Flatté, to be published, J. Vac. Sci. Technol.
7. "Differential gain, differential index, and linewidth enhancement factor for a 4-micron superlattice laser active layer," S. A. Anson, J. T. Olesberg, Michael E. Flatté, T. C. Hasenberg, and Thomas F. Boggess, J. Appl. Phys. **86**, 713 (1999).
8. "Carrier recombination rates in narrow-gap semiconductor superlattices," Michael E. Flatté, C. H. Grein, T. C. Hasenberg, S. A. Anson, D. -J. Jang, J. T. Olesberg, and Thomas F. Boggess, Phys. Rev. B **59**, 5745 (1999).
9. "Optimization of active regions in mid-infrared lasers," J. T. Olesberg, Michael E. Flatté, B. J. Brown, C. H. Grein, T. C. Hasenberg, S. A. Anson, and Thomas F. Boggess, Appl. Phys. Lett. **74**, 188 (1999).
10. "Experimental and theoretical density-dependent absorption spectra in (GaInSb/InAs)/AlGaSb superlattice multiple quantum wells," J. T. Olesberg, S. A. Anson, S. W. McCahon, M. E. Flatté, Thomas F. Boggess, D. H. Chow, and T. C. Hasenberg, Appl. Phys. Lett. **72**, 229 (1998).
11. "Inapplicability of a simply parametrized threshold current in Sb-based IR lasers", C. H. Grein, Michael E. Flatté, and H. Ehrenreich, SPIE Proceedings **3284**, 325 (1998).
12. "Theoretical performance of mid-infraredbroken-gap multilayer superlattice lasers," Michael E. Flatté, C. H. Grein, and J. T. Olesberg, Proceedings of the Materials Research Society, **484**, 71 (1998). (invited)

13. "Sensitivity of mid-infrared InAs/InGaSblaser active regions to temperature and compositionvariations," Michael E. Flatté, C. H. Grein, and H. Ehrenreich, Appl. Phys. Lett., **72**, 1424 (1998).
14. "Auger optimization in mid-infrared lasers: the importance of final-state optimization," Michael E. Flatté and C. H. Grein, Optics Express **2**, 131 (1998). (invited)
15. "Temperature dependence of Auger recombination in a multilayer, narrow-band-gap superlattice," D.-J. Jang, Michael E. Flatté, C. H. Grein, J. T. Olesberg, T. C. Hasenberg, and Thomas F. Boggess, Phys. Rev. B **58**, 14047 (1998).
16. "Auger recombination in antimony-based, strain-balanced, narrow-band-gap superlattices," J. T. Olesberg, Thomas F. Boggess, S. A. Anson, D.-J. Jang, M. E. Flatté, T. C. Hasenberg, and C. H. Grein, in Infrared Applications of Semiconductors II, D. L. McDaniel, Jr., M. O. Manasreh, R. H. Miles, and S. Sivananthan, Eds. (Materials Research Society, Warrendale, PA, 1998) pp. 83 - 88.
17. "III-V Interband 5.2 micron laser operating at 185K," M. E. Flatté, T. C. Hasenberg, J. T. Olesberg, S. A. Anson, Thomas F. Boggess, Chi Yan, D. L. McDaniel, Jr., Appl. Phys. Lett. **71**, 3764 (1997).

INVITED PRESENTATIONS RESULTING FROM THIS PROGRAM

1. "Electronic structure engineering of mid-infrared semiconductor lasers," Michael E. Flatté, J. T. Olesberg, and C. H. Grien, to be presented at a meeting of the Royal Society of London, July 19, 2000.
2. " Electronic structure engineering in mid-IR lasers," Michael E. Flatté, J. T. Olesberg, C. H. Grein, S. A. Anson, T. F. Boggess, and T. C. Hasenberg, LEOS 1999, San Francisco, CA, November 10, 1999.
3. " MWIR Interband Lasers Employing Sb-based Broken-gap Superlattices and Quantum Wells," T. C. Hasenberg, T. F. Boggess, M. E. Flatté, J. T. Olesberg, and C. H. Grein, International Conference on Mid-infrared Optoelectronics --Materials and Devices, Aachen, Germany, September 1999.
4. " Electronic structure engineering in mid-IR lasers," Michael E. Flatté, J. T. Olesberg, C. H. Grein, S. A. Anson, T. F. Boggess, and T. C. Hasenberg,Optical Society of America's Integrated Photonics Research '99 Conference, Santa Barbara, CA, July 19-21, 1999.
5. "InAs/GaInSb broken-gap quantum wells for MWIR diode lasers," Thomas F. Boggess, Michael E. Flatté, T. C. Hasenberg, J. T. Olesberg, Diode Laser Technology Review, Fort Walton Beach, FL, May 12, 1999.
6. "MWIR interband lasers employing broken-gap superlattices and quantum wells, T. C. Hasenberg, T. F. Boggess, M. E. Flatté, J. T. Olesberg, and C. H. Grein, Quantum Optoelectronics Conference, Snowmass Village, CO, April 12-16, 1999.
7. "Ultrafast measurements of optical properties and carrier dynamics in mid-IR semiconductor laser materials," Thomas F. Boggess, Michael E. Flatté, T. C. Hasenberg, S. A. Anson, D.-J. Jang, and J. T. Olesberg, Materials Research Society Meeting, Boston, Dec 1998.
8. "Time-resolved spectroscopy of mid-IR laser structures," Thomas F. Boggess, Second Workshop on Characterization, Future Opportunities and Applications of 6.1Å III-V Semiconductors, Naval Research Laboratory, Washington, DC, August 24-26, 1998.

9. "Electronic structure engineering for antimony-based optical devices," Michael E. Flatt\'e, C.~H.~Grein, and H.~Ehrenreich, Second Workshop on Characterization, Future Opportunities and Applications of 6.1Å III-V Semiconductors, Washington, D.C., August 25, 1998.
10. "Optimization of active region thickness in mid-infrared lasers," Michael E. Flatté, LEOS Workshop on Semiconductor Lasers, San Francisco, CA, May 8, 1998.
11. "Electrically and optically pumped mid-IR lasers using strain-balanced superlattice active regions" Thomas F. Boggess, T. C. Hasenberg, M. E. Flatté. J. T. Olesberg, D.-J. Jang, W. K. Chan, S. A. Anson, B. L. Carter, C. H. Grein, and D. L. McDaniel, Jr., 1998 Diode Laser Technology Review, Albuquerque, NM, March 2-4 1998.
12. Michael E. Flatté, C. H. Grein, and J. T. Olesberg, "Theoretical performance of mid-infrared broken-gap multilayer superlattice lasers," Materials Research Society Meeting, Boston, Dec. 1997.

REFERENCES

[1] S. W. McCahon, S. A. Anson, D.-J. Jang, and Thomas F. Boggess, Opt. Lett. **20**, 2309 (1995).
[2] J. Shah, IEEE J. Quantum Electron. **QE-24**, 276 (1988).
[3] D.-J. Jang, J.T. Olesberg, M.E. Flatté, T.F. Boggess, and T.C. Hasenberg, Appl. Phys. Lett. **70**, 1125 (1997).
[4] M. E. Flatté, C. H. Grein, H. Ehrenreich, R. H. Miles, and H. Cruz, J. Appl. Phys. **78**, 4552 (1995); C. H. Grein, P. M. Young, and H. Ehrenreich, J. Appl. Phys. **76**, 1940 (1994).
[5] Michael E. Flatté, J. T. Olesberg, S. A. Anson, and Thomas F. Boggess, T. C. Hasenberg, R. H. Miles, and C. H. Grein, Appl. Phys. Lett. **70**, 3212 (1997).
[6] T.C. Hasenberg, D.H. Chow, A.R. Kost, R.H. Miles, and L. West, Electron. Lett. **31**, pp. 275-276, Feb. 1995.
[7] T. C. Hasenberg, R. H. Miles, A. R. Kost, and L. West, IEEE J. Quantum Electron. **33**, 1403 (1997).
[8] M. E. Flatté, T. C. Hasenberg, J. T. Olesberg, S. A. Anson, Thomas F. Boggess, Chi Yan, and D. L. McDaniel, Jr., Appl. Phys. Lett. **71**, 3764 (1997).
[9] J. T. Olesberg, S. A. Anson, S. W. McCahon, Michael E. Flatté, D. H. Chow, and T. C. Hasenberg, *Appl. Phys. Lett.* **72**, 229 (1998).
[10] S. A. Anson, J. T. Olesberg, Michael E. Flatté, T. C. Hasenberg, and Thomas F. Boggess, *J. Appl. Phys.* **86**, 713 (1999).
[11] D.-J. Jang, M.E. Flatté, C.H. Grein, J.T. Olesberg, T.C. Hasenberg, T.F. Boggess, Phys. Rev. B**58**, 13047 (1998).
[12] Michael E. Flatté and C. H. Grein, *Optics Express* **2**, 131 (1998).
[13] J. R. Meyer, C. A. Hoffman, F. J. Bartoli, and L. R. Ram-Mohan, Appl. Phys. Lett. **67**, 757 (1995).
[14] J. T. Olesberg, Michael E. Flatté, B. J. Brown, C. H. Grein, T. C. Hasenberg, S. A. Anson, and Thomas F. Boggess, *Appl. Phys. Lett.* **74**, 188 (1999); J. T. Olesberg, Michael E. Flatté, B. J. Brown, T. C. Hasenberg, S. A. Anson, Thomas F. Boggess, and C. H. Grein, in *In-Plane Semiconductor Lasers III*, edited by Hong K. Choi and Peter S. Zory, SPIE Proceedings Vol. **3628** (The International Society for Optical Engineering, Bellingham, 1999), pg. 148.
[15] D. Z. Garbuzov, R. U. Martinelli, H. Lee, P. K. York, R. J. Menna, J. C. Connolly, and S. Y. Narayan, *Appl. Phys. Lett.* **69**, 2006 (1996); D. Z. Garbuzov, R. U. Martinelli, H. Lee, R. J. Menna, P. K. York, L. A. DiMarco, M. G. Harvey, R. J. Matarese, S. Y. Narayan, and J. C. Connolly, *Appl. Phys. Lett.* **70**, 2931 (1997); D. Z. Garbuzov, H. Lee, V. Khalfin, R. Martinelli, J. C. Connolly, and G. L. Belenky, *IEEE Photon. Technol. Lett.* **11**, 794 (1999).
[16] W. W. Bewley, C. L. Felix, E. H. Aifer, I. Vurgaftman, L. J. Olafsen, J. R. Meyer, H. Lee, R. U. Martinelli, J. C. Connolly, A. R. Sugg, G. H. Olsen, M. J. Yang, B. R. Bennett, and B. V. Shanabrook, *Appl. Phys. Lett.* **73**, 3833 (1998).
[17] H. Q. Le, C. H. Lin, S. J. Murray, R. Q. Yang, and S. S. Pei, *IEEE J. Quantum Electron.* **34**, 1016 (1998).
[18] L. A. Coldren and S. W. Corzine, *Diode lasers and photonic integrated circuits,* (Wiley, NY, 1995).

[19] C.L. Felix, W.W. Bewley, I Vurgaftman, L.J. Olafsen, D.W. Stokes, J.R. Meyer, and M.J. Yang, Appl. Phys. Lett. **75**, 2876 (1999).

[20] C. H. Henry, IEEE J. Quantum Electron. **18**, 259, 1982.

[21] F. Kano, Y. Yoshikuni, M. Fukuda, and J. Yoshida, IEEE Photon. Technol. Lett. **3**, 877 (1991); Fumiyoshi Kano, Takayuki Yamanaka, Norio Yamamoto, Hiroyasu Mawatari, Yuichi Tohmori, and Yuzo Yoshikuni, IEEE J. Quantum Electron. **30**, 533 (1994).

[22] Takayuki Yamanaka, Yuzo Yoshikuni, Wayne Lui, Kiyoyuki Yokoyama, and Shunji Seki, Appl. Phys. Lett. **62**, 1191 (1993); Takayuki Yamanaka, Yuzo Yoshikuni, Wayne Lui, Kiyoyuki Yokoyama, and Shunji Seki, IEEE J. Quantum Electron. **29**, 1609 (1993).

[23] Marek Osinski, Jens Buus, IEEE J. Quantum Electron. **23**, 9 (1987).

[24] Sang S. Lee, Luis Figueroa, and Ramu Ramaswamy, IEEE J. Quantum Electron. **25**, 862 (1989).

[25] Tsukuru Ohtoshi and Naoki Chinone, IEEE Photon. Technol. Lett. **1**, 117 (1989).

[26] Westbrook, L. D., Electron. Lett. **21**, 1018 (1985).

[27] Igor Vurgaftman and Jerry R. Meyer, J. Select. Topics Quantum Electron. **3**, 475 (1997).

[28] Jérôme Faist, Federico Capasso, Carlo Sirtori, Deborah L. Sivco, Albert L. Hutchinson, and Alfred Y. Cho, Appl. Phys. Lett. **67**, 3057 (1995).

[29] H. K. Choi and G. W. Turner, Appl. Phys. Lett. **67**, 332 (1995).

[30] The structure used is taken from Fig. 1 of S. R. Kurtz, A. A. Allerman, and R. M. Biefeld, Appl. Phys. Lett. **70**, 3188 (1997). Values for the strained bulk band gaps and band offsets are taken from the figure.

[31] Michael E. Flatté, C. H. Grein, T. C. Hasenberg, S. A. Anson, D.-J. Jang, J. T. Olesberg, and Thomas F. Boggess, Phys. Rev. B 59, 5745 (1999).

[32] J. I. Malin, J. R. Meyer, C. L. Felix, J. R. Lindle, L. Goldberg, C. A. Hoffman, F. J. Bartoli, C.-H. Lin, P. C. Chang, S. J. Murray, R. Q. Yang, and S.-S. Pei, Appl. Phys. Lett. **68**, 2976 (1996).

[33] K. Furuya, Electron. Lett. **21**, 200 (1985).

[34] J. T. Olesberg, S. A. Anson, S. W. McCahon, Michael E. Flatté, Thomas F. Boggess, D. H. Chow, and T. C. Hasenberg, Appl. Phys. Lett. **72**, 229 (1998); D.-J. Jang, Michael E. Flatté, C. H. Grein, J. T. Olesberg, T. C. Hasenberg, and Thomas F. Boggess, Phys. Rev. B **58**, 13047 (1998).

[35] The ratio of the zone center masses, $\left(m_v / m_c\right)^{3/2}$, could also be used to quantify the density of states imbalance, but it does not account for the strong nonparabolicity of the valence band or the presence of multiple valence subbands.

[36] Gilad Almogy, Mordechai Segev, and Amnon Yariv, Opt. Lett. **19**, 1192 (1994).

[37] S. W. McCahon, S. A. Anson, D.-J. Jang, M. E. Flatté, Thomas F. Boggess, D. H. Chow, T. C. Hasenberg, C. H. Grein, Appl. Phys. Lett. **68**, 2135 (1996).

[38] M. E. Flatté, C. H. Grein, and H. Ehrenreich, Appl. Phys. Lett. **72**, 1424 (1998).

[39] See, e.g., G. P. Agrawal and N. K. Dutta, Semiconductor Lasers, 2nd Edition (ITP Van Nostrand, New York, 1993).

[40] See, e.g., S. Hauser, G. Fuchs, A. Hangleiter, K. Streubel, and W. T. Tsang, Appl. Phys. Lett. **56**, 913 (1990).

[41] Yao Zau, Julian S. Osinski, Piotr Grodzinski, P. Daniel Dapkus, William C. Rideout, W. F. Sharfin, J. Schlafer, and F. D. Crawford, J. IEEE Quantum Electron. **QE-29**, 1565 (1993); F. Fuchs, C. Schiedel, A. Hangleiter, V. Härle, and F. Scholz, Appl. Phys. Lett. **62**, 396 (1993).

[42] Shunji Seki,Wayne W. Lui, and Kiyoyuki Yokoyama, Appl. Phys. Lett. **66**, 3093 (1995).

[43] J. R. Lindle, J. R. Meyer, C. A. Hoffman, F. J. Bartoli, G. W. Turner, and H. K. Choi, Appl. Phys. Lett. **67**, 3153 (1995).

[44] C. L. Felix, J. R. Meyer, I. Vurgaftman, C.-H. Lin, S. J. Murry, D. Zhang, and S.-S. Pei, IEEE Photonics Technol. Lett. **9**, 734 (1997).

[45] W. W. Bewley, I Vurgaftman, C. L. Felix, J. R. Meyer, C.-H. Lin, D. Zhang, S. J. Murry, S.-S. Pei, L. R. Ram-Mohan, J. Appl. Phys. **83**, 2384 (1998).

[46] The authors indicate that this behavior may be an artifact of their analysis resulting from an overestimation of the threshold carrier density.

[47] P. Asbeck, J. Appl. Phys. **48**, 820 (1977).

[48] J. T. Olesberg, Thomas F. Boggess, S. A. Anson, D.-J. Jang, M. E. Flatté, T. C. Hasenberg, and C. H. Grein, Mat. Res. Soc. Symp. Proc. **484**, 83 (1998).

[49] C. H. Grein, P. M. Young, M. E. Flatté, and H. Ehrenreich, J. Appl. Phys. **78,** 7143 (1995).

[50] R. Peierls, Ann. Phys. (Leipzig) **12**, 154 (1932).

[51] C. A. Hoffman, J. R. Meyer, E. R. Youngdale, F. J. Bartoli, and R. H. Miles, Appl. Phys. Lett. **63**, 2210 (1993).
[52] A. Y. Lew, S. L. Zuo, E. T. Yu, and R. H. Miles, Phys. Rev. B **57**, 6534 (1998).
[53] J. R. Meyer, C. L Felix, W. W. Bewley, I. Vurgaftman, E. H. Aifer, L. J.Olafsen, J. R. Lindle, C. A. Hoffman, M.-J. Yang, B. R. Bennett, B. V. Shanabrook, H. Lee, C. -H. Lin, S. S. Pei, and R. H. Miles, Appl. Phys. Lett. **57**, 801 (1998).
[54] H. J. Eichler, P. Gunter, and D. W. Pohl in *Laser-Induced Dynamic Gratings*, (Springer, Berlin, 1986).
[55] S. C. Moss, J. R. Lindle, H. J. Mackey, and A. L. Smirl, Appl. Phys. Lett. **39**, 227 (1981).
[56] J. Hegarty, M. D. Sturge, A. C. Gossard, and W. Wiegmann, Appl. Phys. Lett. **40**, 132 (1982).
[57] V. Grivickas, V. Netiksis, D. Noreika, M. Petrauskas, M. Willander, W.-X. Ni, M.-A. Hasan, G. V. Hansson, and J.-E. Sundgren, J. Appl. Phys. **70**, 1471 (1991).
[58] A. Miller, R. J. Manning, P. K. Milsom, D. C. Hutchings, D. W. Crust, and K. Woodbridge, J. Opt. Soc. Am B **6**, 567 (1989).
[59] X. R. Huang, D. S. McCallum, M. D. Dawson, A. L. Smirl, T. F. Boggess, T. C. Hasenberg, and R. L. Tober, J. Appl. Phys. **74**, 1868 (1993).
[60] J. R. Meyer, personal communication.
[61] H. Sakaki, T. Noda, K. Hirakawa, M. Tanaka, and T. Matsusue, Appl. Phys. Lett. **51**, 1924 (1987).
[62] G. W. Turner and H. K. Choi, personal communication.

DISTRIBUTION LIST

DTIC/OCP
8725 John J. Kingman Rd, Suite 0944
Ft Belvoir, VA 22060-6218 1 cy

AFSAA/SAMI
1570 Air Force Pentagon
Washington, DC 20330-1570 1 cy

AFRL/VSIL
Kirtland AFB, NM 87117-5776 2 cys

AFRL/VSIH
Kirtland AFB, NM 87117-5776 1 cy

The University of Iowa
Division of Sponsored Programs
2 Gilmore Hall
Iowa City, IA 52242 1 cy

Official Record Copy
AFRL/DELS/Sylvia Dorato 3 cys